A wavelet-based method for multifractal image analysis. II. Applications to synthetic multifractal rough surfaces

N. Decoster[1], S.G. Roux[1,2], and A. Arnéodo[1,a]

[1] Centre de Recherche Paul Pascal, Avenue Schweitzer, 33600 Pessac, France
[2] Climate & Radiation Branch, NASA's Goddard Space Flight Center, Greenbelt, Maryland 20771, USA

Abstract. We apply the 2D wavelet transform modulus maxima (WTMM) method to synthetic random multifractal rough surfaces. We mainly focus on two specific models that are, *a priori*, reasonnable candidates to simulate cloud structure in paper III (S.G. Roux, A. Arnéodo, N. Decoster, Eur. Phys. J. B **15**, 765 (2000)). As originally proposed by Schertzer and Lovejoy, the first one consists in a simple power-law filtering (known in the mathematical literature as "fractional integration") of singular cascade measures. The second one is the foremost attempt to generate log-infinitely divisible cascades on 2D orthogonal wavelet basis. We report numerical estimates of the $\tau(q)$ and $D(h)$ multifractal spectra which are in very good agreement with the theoretical predictions. We emphasize the 2D WTMM method as a very efficient tool to resolve multifractal scaling. But beyond the statistical information provided by the multifractal description, there is much more to learn from the arborescent structure of the wavelet transform skeleton of a multifractal rough surface. Various statistical quantities such as the self-similarity kernel and the space-scale correlation functions can be used to characterize very precisely the possible existence of an underlying multiplicative process. We elaborate theoretically and test numerically on various computer synthetized images that these statistical quantities can be directly extracted from the considered multifractal function using its WTMM skeleton with an arbitrary analyzing wavelets. This study provides algorithms that are readily applicable to experimental situations.

PACS. 47.53.+n Fractals – 05.40.-a Fluctuations phenomena, random processes, noise, and Brownian motion – 07.05.Pj Image processing – 68.35.Bs Surface structure, and topography

1 Introduction

Multiplicative cascade models have enjoyed increasing interest in recent years as the paradigm of multifractal objects [1–5]. The notion of cascade actually refers to a self-similar process whose properties are defined multiplicatively from coarse to fine scales. In that respect, it occupies a central place in the statistical theory of turbulence [4,6,7]. Since Richardson's famous poem [8], the turbulent cascade picture has been often invoked to account for the intermittency phenomenon observed in fully developed turbulent flows [6–11]: energy is transferred from large eddies down to small scales (where it is dissipated) through a cascade process in which the transfer rate at a given scale is not spatially homogeneous, as supposed in the theory developed by Kolmogorov [12] in 1941, but undergoes local intermittent fluctuations [6,7,10,11]. Over the past fourty years, refined models including the log-normal model of Kolmogorov [13] and Obukhov [14], multiplicative hierarchical cascade models like the random β-model [15], the α-model [16], the p-model [17] (for a review, see Ref. [4]), the log-stable models [18–20] and more

recently the log-infinitely divisible cascade models [21–24] with the rather popular log-Poisson model advocated by She and co-workers [22,25], have grown in the literature as reasonable models to mimic the energy cascading process in turbulent flows. On a very general ground, a self-similar cascade is defined by the way the scales are refined and by the statistics of the multiplicative factors at each step of the process [4,5,20]. One can thus distinguish discrete cascades that involve discrete scale ratios leading to log-periodic corrections to scaling (discrete scale invariance [26–28]), from continuous cascades without preferable scale factor (continuous scale invariance). As far as the fragmentation process is concerned, one can specify whether some conservation laws are operating or not [5]; in particular, one can discriminate between conservative (the measure is conserved at each cascade step) and non conservative (only some fraction of the measure is transfered at each step) cascades. More fundamentally, there are two main classes of self-similar cascade processes: deterministic cascades that generally correspond to solvable models and random cascades that are likely to provide more realistic models but for which some theoretical care is required as far as their multifractal limit and some basic multifractal properties (including multifractal phase

[a] e-mail: `arneodo@crpp.u-bordeaux.fr`

transitions) are concerned [5]. As a notable member of the later class, the independent random cascades introduced by Mandelbrot (commonly called $\mathcal{M}$-cascades [9,29]) as a general model of random curdling in fully developed turbulence, have a special status since they are the main cascade model for which deep mathematical results have been obtained [30,31]. Note that most of these 1D cascade models have natural generalization in 2D and higher dimensions. Since realistical turbulent systems (*e.g.* atmospheric turbulence [32]) are likely to display anisotropic scaling, full realism requires the possibility of introducing spatial anisotropy [18,20,32–34]. Moreover, as pointed out by Schertzer and Lovejoy [33], this "first generation" of cascade models is static in the sense that it accounts for the multiplicative hierarchical structure of the data in the spatial domain only [20]. With the specific goal to model temporal evolution, these authors have proposed a "second generation" of space-time cascade models that take into account both the scaling anisotropy between space and time, and the breaking of the mirror symmetry along the temporal axis, *i.e.*, causality [20,33,34]. For the basic framework necessary to handle space-time anisotropic scaling, we refer the reader to references [20,34], where the concepts of Generalized Scale Invariance (GSI) and space-time multifractals have been introduced and explored.

However, in physics as well as in other applied sciences, fractals appear not only as singular measures but also as singular functions [1,7,32,35–45]. For instance in fully developed turbulence, directly observable quantities are the velocity field or the temperature field rather than the dissipation field [6,7,10,11]. Paradoxically, if there is a plethora of mono and multifractal cascade models in the literature that generate deterministic as well as random singular measures in the small-scale limit, there are still only a handful of distinct algorithms for synthesizing "rough" functions of a single variable with multifractal statistics. Beyond the problem of the multifractal description of singular functions that has been solved with the WTMM method [46–50], there is thus the practical issue of defining in any concrete way how to build a multifractal function. Schertzer and Lovejoy [18] suggested a simple power-law filtering (fractional integration) of singular cascade measures. So, this model combines a multiplicative procedure with an additive one reminiscent of some algorithms to generate fractional Brownian motion (fBm) [1,51,52]. In the same spirit, the bounded cascade model of Marshak *et al.* [53] consists in acting on the multiplicative weights during the cascade in physical space, to recover continuity in the small-scale limit. In references [54,55], the midpoint displacement technique for building fBm was generalized to generate deterministic or random multi-affine functions. The same goal was achieved in references [47,48] by combining fractional or ordinary integration with signed measures obtained by recursive cascade like procedures. Several other attempts to simulate "synthetic turbulence" that shares the intermittency properties of turbulent velocity data have partially succeeded [56–59]. More recently, the concept of self-similar cascades leading to multifractal measures has

been generalized to the construction of scale-invariant signals using orthonormal wavelet basis [60–63]. Instead of redistributing the measure over sub-intervals with multiplicative weights, one allocates the wavelet coefficients in a multiplicative way on the dyadic grid. This method has been implemented to generate multifractal functions from a given deterministic or probalistic multiplicative process. From a mathematical point of view, the convergence of these $\mathcal{W}$-cascades and the regularity properties of the so-obtained deterministic or stochastic functions have been discussed by one of us (A.A.) and co-workers in reference [64].

Coming to rough surfaces generated by fractal functions of two variables, we are aware of various algorithms for fBm surface generation [51,52,65–67]. We have listed these algorithms in paper I [68] and shown that the rough surfaces simulated with those additive processes display homogeneous monofractal scaling properties as described by a unique scaling exponent, namely the Hurst exponent. To the best of our knowledge, only two algorithms for multifractal functions of two variables have been documented, to some extend, in publications. Both were developed with atmospheric applications in mind and correspond to straightforward generalizations in 2D of the fractionally integrated singular cascade models [18,20,69,70] and the "bounded cascade model" [71,72] mentioned just above. But our purpose here is far from being restricted to turbulence and to possible geophysical applications (this issue will be addressed in paper III [73]). Actually our first main objective is to explore ways of generating multifractal rough surfaces with prescribed multifractal statistics along the path open by the random $\mathcal{W}$-cascades on wavelet dyadic trees in references [60–64]. The idea is to introduce a new class of square integrable (finite energy) functions over the real plane $\mathbb{R}^2$, using a separable 2D wavelet orthogonal basis [74–76]. The multifractal scaling properties are recovered from the multiplicative process used to generate the wavelet coefficients: these functions are built recursively in the orthogonal wavelet space-scale representation, "cascading" from an arbitrary given large scale towards small scales. These 2D random $\mathcal{W}$-cascade models present two crucial advantages as far as future research is concerned. From a theoretical point of view, the fact of using wavelet orthogonal basis provides the framework for some rigorous mathematical treatment. This is out of the scope of the present work but we hope to elaborate about this point in a forthcoming publication. From a practical point of view, the fact of using separable multiresolution schemes provides a simple and very efficient algorithmic procedure for designing and synthesizing multifractal rough surfaces. Let us point out that this multiresolution synthesis algorithm has enough flexibility for making tractable the implementation of anisotropic scale invariance. Since our second and main objective in this paper is to test the reliability of the 2D WTMM method introduced in Section 4 of paper I [68], we will copiously use this multi-resolution synthesis algorithm to generate collections of numerical images of multifractal rough surfaces, each collection corresponding to a particular

cascading process (*e.g.*, log-normal process, log-Poisson process, ...). Then, for each set of images, we will compute the $\tau(q)$ and $D(h)$ multifractal spectra with the 2D WTMM method and compare the numerical results with the theoretical predictions. Within the perspective of experimental application of the 2D WTMM method to geophysical data in paper III [73], we will proceed to a comparative multifractal analysis of rough surfaces generated by the fractionally integrated singular cascade model [18, 20, 69, 70].

But from the very analogy that links the multifractal description and statistical thermodynamics [2, 49, 77–79], there still exists some fundamental insufficiency in the determination of the multifractal spectra. In particular, $\tau(q)$ and $D(h)$ play respectively the role of thermodynamical potentials, namely free energy and entropy, which intrinsically contain only some degenerate information about the "Hamiltonian" of the problem, *i.e.*, the underlying cascading process [80, 81]. Therefore, it is not surprising that previous experimental determinations of the $\tau(q)$ and $D(h)$ spectra of turbulent fields, have failed to provide a selective test to discriminate between existing (deterministic or random) cascade models. In order to go beyond the classical multifractal description, Castaing and co-workers [24, 82–88] have proposed some approach of the intermittency phenomenon which amounts to model the evolution of the shape of the turbulent velocity increment probability density function (pdf), from Gaussian at large scales to more intermittent profiles with stretched exponential-like tails at smaller scales [82, 89–92], by a functional equation that relates two scales using a kernel G. This self-similarity kernel actually contains deep information on the underlying multiplicative process: its shape is determined by the nature of the elementary step in the cascade, while the way G depends on the coarse and fine scales reflects the scale invariance properties of the cascade. In their original work, Castaing *et al.* [24, 82–87] mainly focused on the estimate of the variance of G and its scale behavior. A generalization of this approach to the wavelet transform of the velocity field has been proposed in a previous work and shown to provide direct access to the entire shape of the kernel G [61–63, 81]. This wavelet-based method has been tested on synthetic 1D turbulent signals and further applied to turbulence data. At the highest accessible Reynolds numbers, the computation of the self-similarity kernel G yields a very convincing log-normal law on a well defined range of scales that can be further used as an objective definition of the inertial range [62, 63, 81]. Moreover, the number of cascade steps is found to evolve as a power-law (and not logarithmically) as a function of the scale, which is the signature of the breaking of scale-invariance [62, 63, 81, 93]. However, the investigation of data sets recorded at different Reynolds numbers suggests the asymptotic validity of the log-normal multifractal description [63, 81, 93].

As emphasized in a recent work [94], one can and one must go even deeper in the multifractal analysis by studying correlation functions in both space and scales. The wavelet transform skeleton defined by the wavelet

transform modulus maxima actually contains the key space-scale information required for this "two-point" statistical analysis. In the arborescent structure of the wavelet transform is somehow uncoded the underlying multiplicative cascade process [81, 94–96]. The computation of the space-scale correlations functions from the wavelet transform skeleton has been proved to provide conclusive evidence for the existence of some internal ultrametric structure [94]. We refer the readers to references [81, 94, 97] for preliminary applications of this wavelet based space-scale correlation method to fully developed turbulence data and financial time-series. Our third goal in this paper, is to generalize the self-similarity kernel and space-scale correlation function approaches to the statistical study of multifractal rough surfaces. Part of the work will consist in adapting the mathematical concepts and in turn enriching our algorithmic park from 1D to 2D analysis. The final touch will be test applications of the corresponding softwares to numerical synthetic images generated by 2D random $\mathcal{W}$-cascade processes for which the self-similarity kernel as well as the space-correlation functions are known analytically.

The paper is organized as follows. In Section 2, we describe the 2D versions of the fractionally integrated singular cascade model and of the random $\mathcal{W}$-cascade process on separable wavelet orthogonal basis. These models can be used to synthesize rough surfaces that display multifractal scaling properties with prescribed $\tau(q)$ and $D(h)$ spectra. In Section 3, we report the results of test applications of the 2D WTMM method introduced in Section 4 of paper I [68], to previously synthesized multifractal rough surfaces. Our main goal is to calibrate our numerical tools with respect to finite-size effects and statistical convergence. Sections 4 and 5 are respectively devoted to the generalization in 2D of the self-similarity kernel and space-scale correlation function methods [81]. We illustrate our purpose with numerical applications which confirm the necessity of investigating "two-point" statistics across scales to get definite and conclusive evidence for a multiplicative hierarchical structure underlying the roughness fluctuations of multifractal surfaces. We conclude in Section 6 by discussing the wide range of potential applications of this 2D wavelet-based statistical analysis in fundamental as well as in applied sciences, from image processing to image synthesis, from numerical to experimental data analysis.

2 Hierarchical models for multifractal rough surface synthesis

There are many well documented methods for generating multifractal measures using multiplicative cascades [9, 13–25, 32–34]. In contrast, the literature on specific ways of synthesizing multifractal functions is relatively small [18, 47, 48, 53–64, 98]. We present two procedures here: the first one, the Fractionally Integrated Singular Cascade (FISC) has been introduced and plentifully applied for multifractal geophysical field modeling [18, 20, 69, 70, 99–101]; the second one is
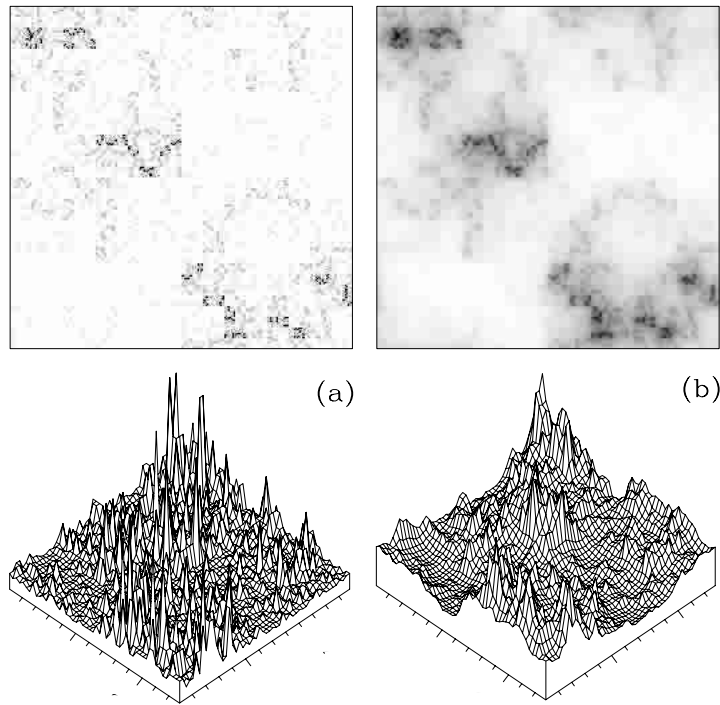
Fig. 1. (a) Multifractal measure generated using the binomial cascade model with the parameter value $p = 0.32$. (b) Multifractal rough surface obtained after fractional integration with an exponent $H^* = 0.638$. In the top (1024×1024) panels, $\mu(\mathbf{x})$ and $f(\mathbf{x})$ are coded using 32 grey levels from white (min μ or min f) to black (max μ or max f).

quite original since it consists in generating multifractal rough surfaces from random cascade process on separable wavelet orthogonal basis.

2.1 Fractionally integrated singular cascades

A stochastic model with continuously variable intermittency was originally proposed by Schertzer and Lovejoy for rain (1D), clouds (2D), landscapes (2D) or any other compliant multifractal geophysical fields [18,20,69,70,72,101]. The idea is to start with a specific model of singular multiplicative cascade and then to proceed to a straightforward filtering in Fourier space (fractional integration) in order to bring multifractal measures into the realm of continuous multifractal functions. Let us note that this strategy is strongly inspired from the devil's staircase concept which is nothing but a straightforward integration of some Bernoulli measure distributed on a Cantor set [1,47–49].

A multiplicative cascade process consists in starting with some 2D spatial domain, let say a square of characteristic size L, on which a measure $\mu = \mu_L$ is uniformly distributed. At the first step of the construction, the initial domain breaks into smaller domains, let say the initial square breaks into four smaller squares of characteristic size $L/2$, each receiving a fraction of the original measure as defined by a random variable M with a certain probability distribution $P(M)$. By repeating the same procedure recursively at smaller scales using independent realizations of the random variable M, one generates a random singu-

lar measure over the $L \times L$ square:

$$\mu_n(\mathbf{x}; l) = \mu_L \prod_{i=1}^{n} M_i , \;\; l/L = 2^{-n} \to 0 . \tag{1}$$

Since the cascading process is space-filling, all the information on the singular nature of this multiplicative process is contained in the specific shape of the so-called "measure multiplier" [4,9] probability distribution. In the present study, we will mainly focus on the "p-model" (also called "binomial model") originally proposed by Meneveau and Sreenivasan [17] to simulate the highly intermittent fluctuations of the kinetic energy dissipation field in fully developed turbulence. In this model, $P(M)$ has the following simple form [4,17]:

$$P(M) = 1/2\Big\{\delta\big(M - M^{(1)}\big) + \delta\big(M - M^{(2)}\big)\Big\} , \tag{2}$$

where

$$M^{(1)} = p/2 , \; M^{(2)} = (1-p)/2 , \; 0 \le p \le 1/2 , \tag{3}$$

independently of the cascade step. For the present discussion, we additionally impose conservation of the measure at each step; this means that one selects at random among the 4 sub-squares, the two which will receive a fraction $M^{(1)} = p/2$, the two others receiving the fraction $M^{(2)} = (1-p)/2$ of the measure at the previous step. A straightforward computation (see Refs. [4,17], for detailed calculations) of the $\tau(q)$ spectrum defined in Section 4.1 of paper I [68] (Eqs. (59, 60)) yields:

$$\tau_\mu(q) = -(q+1) - \log_2\big(p^q + (1-p)^q\big) . \tag{4}$$
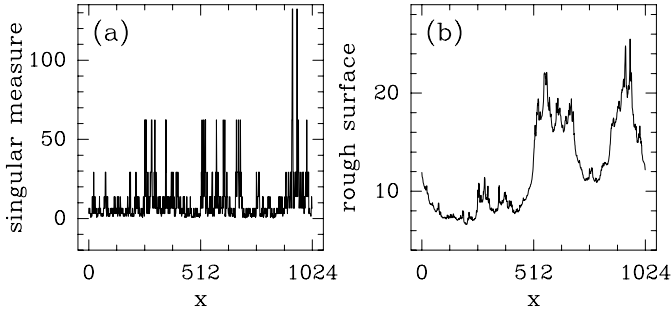
Fig. 2. 1D profiles obtained along some horizontal cut in Figures 1a and 1b respectively: (a) μ *vs.* x; (b) f *vs.* x.

When $p \neq 1/2$ ($p = 1/2$ corresponds to a uniform distribution of the measure over the original square), one gets a nonlinear $\tau(q)$ spectrum which is the hallmark of multifractal scaling properties. Figure 1a shows a realisation of such a random measure for the parameter value $p = 0.32$ after 10 cascade steps. The intense spikiness is witness to the singularity of this binomial cascade model. The intermittent character of this measure is clearly seen on 1D cuts as illustrated in Figure 2a. In the limit of an infinite number of steps, we are clearly not dealing with a function of $(x, y) \in [0, L]^2$: the product $\prod_{i=1}^{n} M_i$ in equation (1) is generally zero but infinite just often enough to keep the domain average at unity.

As a mean of introducing continuity, the form of fractional integration we use here, is a low-pass power-law filtering in Fourier space [18,20]. The measure $\mu_n(\mathbf{x})$ is "smoothed" into a function using:

$$f_n(\mathbf{x}) = \mu_n(\mathbf{x}) * |\mathbf{x}|^{-(1-H^*)} , \ 0 < H^* < 1 \qquad (5)$$

i.e., in Fourier space

$$\hat{f}_n(\mathbf{k}) = A(H^*)\hat{\mu}_n(\mathbf{k}).|\mathbf{k}|^{-H^*} , \qquad (6)$$

where the symbol $*$ denotes the convolution product and

$$A(H^*) = \sqrt{\frac{2}{\pi}} \cos\left(\frac{\pi}{2}H^*\right) \Gamma(H^*) . \qquad (7)$$

Figure 1b shows the result for the same binomial cascade as in Figure 1a but for an order of fractional integration $H^* = 0.638$. The exponent H^* of the power-law filter is chosen so that the function $f(\mathbf{x}) = \lim_{n \to +\infty} f_n(\mathbf{x})$ is continuous everywhere, *i.e.*, the support of its $D(h)$ singularity spectrum (Eqs. (58) and (61) in paper I [68]) does not extend to values lower or equal to zero ($0 \leq h_{\min} \leq h_{\max}$). The intermittent or multifractal character of the corresponding rough surface in Figure 1b is exemplified when looking at the profiles obtained from 1D cuts as illustrated in Figure 2b. A little algebra leads to the following expression for the $\tau(q)$ spectrum of these multifractal random functions [72,99–101]:

$$\tau_f(q) = \tau_\mu(q) + qH^* ,$$
$$= -1 - q(1 - H^*) - \log_2\left(p^q + (1-p)^q\right) . \qquad (8)$$
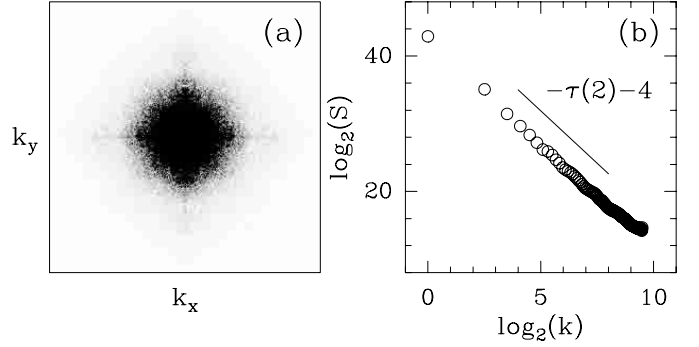
Fig. 3. Power-spectrum analysis of the (1024×1024) image of the fractionally integrated singular cascade shown in Figure 1b. (a) $\ln|\hat{f}_{n=10}(\mathbf{k})|$ as coded using 32 grey levels from white ($\min \ln|\hat{f}|$) to black ($\max \ln|\hat{f}|$). (b) The spectral density $S(|\mathbf{k}|)$ *vs.* $|\mathbf{k}|$ in a logarithmic representation. The solid line corresponds to the theoretical power-law prediction with exponent $\beta = \tau_f(2)+4 = 1+2H^*-\log_2(2p^2-2p+1)$ (Eq. (11)) with $p = 0.32$ and $H^* = 0.638$.

Let us note that for $q = 0$, one finds $\tau_f(0) = -D_F = -2$, *i.e.*, those fractionally integrated rough surfaces are singular everywhere. For $q = 1$, one gets $\tau_f(1) = H^* - 2$, which gives for the fractal dimension of this surface:

$$d_F(\mathcal{S}) = \max(2, 1 - \tau_f(1)) ,$$
$$= \max(2, 3 - H^*) ,$$
$$= 3 - H^* , \qquad (9)$$

i.e., a fractal dimension in between $d_F = 2$ ($H^* = 1$) and 3 ($H^* = 0$). Now from the exponent obtained for $q = 2$, one can derive the scaling exponent β of the spectral density:

$$S(|\mathbf{k}|) \sim |\mathbf{k}|^{-\beta} , \qquad (10)$$

with

$$\beta = \tau_f(2) + 4 ,$$
$$= 1 + 2H^* - \log_2(2p^2 - 2p + 1) . \qquad (11)$$

In Figure 3 are reported the results of a power-spectrum analysis of the (1024×1024) image shown in Figure 1b.

In Figure 3a, the Fourier transform of this image displays some anisotropy along the k_x and k_y axis, which is nothing but the signature of the square lattice anisotropy which underlies the hierarchical construction rule of the singular cascade. Despite this departure from isotropy, the power-spectral density shown in Figure 3b behaves as a power-law as a function of the wavevector modulus $k = |\mathbf{k}|$, with an exponent $\beta = 3.10$ which is in good agreement with the theoretical prediction (11).

From the computation of $\partial \tau_f(q)/\partial q$ in the limits $q \to \pm\infty$ [48,49], one gets the following boundaries for the support of the $D(h)$ singularity spectrum:

$$h_{\min} = \lim_{q \to +\infty} \frac{\partial \tau_f(q)}{\partial q} = H^* - 1 - \log_2(1-p) , \qquad (12)$$
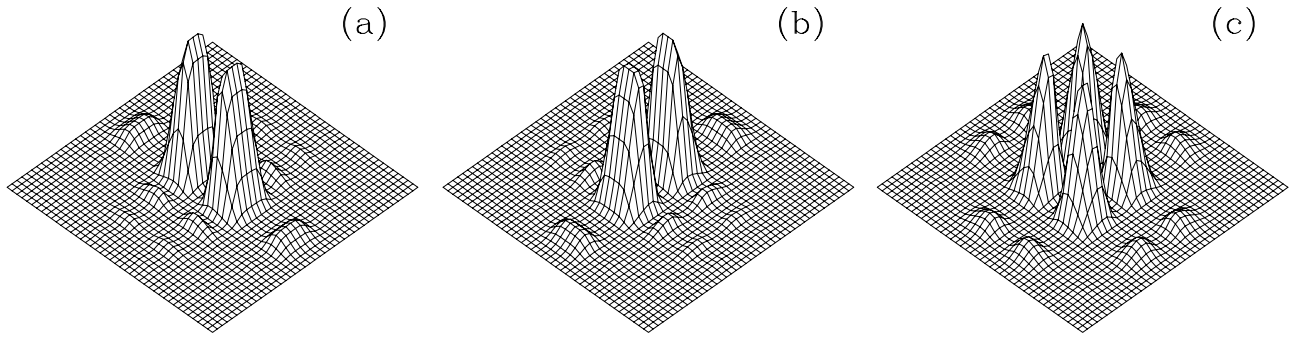
Fig. 4. Fourier transforms of the 3 separable wavelets calculated from a 1D Daubechies 8 wavelet [74]: (a) $\hat{\psi}^1(k_x, k_y)$; (b) $\hat{\psi}^2(k_x, k_y)$; (c) $\hat{\psi}^3(k_x, k_y)$.

and

$$h_{\max} = \lim_{q \to -\infty} \frac{\partial \tau_f(q)}{\partial q} = H^* - 1 - \log_2(p) , \tag{13}$$

where we recall that $0 \leq p \leq 1/2$. For $p = 1/2$, one recovers monofractal scaling with a unique Hölder exponent $h = H^*$. For any other value of the parameter p, one has multifractal scaling with a Hölder exponent h which fluctuates from point to point, taking value in the interval $h \in [h_{\min}, h_{\max}]$.

2.2 Random cascades on separable wavelet orthogonal basis

As mentioned in the introduction, a $\mathcal{W}$-cascade [64] is built recursively on the two-dimensional square grid of separable wavelet orthogonal basis, involving only scales that range between a given large scale L and the scale 0 (excluded). Thus the corresponding fractal function $f(\mathbf{x})$ will not involve scales greater than L. For that purpose, we will use compactly supported wavelets [74].

2.2.1 Two-dimensional wavelet orthogonal basis [74–76]

As in one dimension, the notion of resolution is formalized with orthogonal projections in spaces of various sizes. The approximation of an image $f(\mathbf{x}) = f(x, y)$, at the resolution 2^{-j}, is defined as the orthogonal projection of f on a space $\mathbf{V}_j^2$ that is included in $L^2(\mathbb{R}^2)$. The space $\mathbf{V}_j^2$ is the set of all approximations at the resolution 2^{-j}. When the resolution decreases, the size of $\mathbf{V}_j^2$ decreases as well. Here we consider the particular case of separable multiresolution. Let $\{\mathbf{V}_j\}_{j \in \mathbb{Z}}$ be a multi-resolution of $L^2(\mathbb{R})$. A separable 2D multi-resolution is composed of the tensor product spaces:

$$\mathbf{V}_j^2 = \mathbf{V}_j \otimes \mathbf{V}_j . \tag{14}$$

Let $\mathbf{W}_j^2$ be the detail space equal to the orthogonal complement of the lower resolution approximation space $\mathbf{V}_j^2$

in $\mathbf{V}_{j-1}^2$:

$$\mathbf{V}_{j-1}^2 = \mathbf{V}_j^2 \oplus \mathbf{W}_j^2 . \tag{15}$$

One can rewrite this equation in the following way:

$$\mathbf{V}_{j-1} \otimes \mathbf{V}_{j-1} = (\mathbf{V}_j \otimes \mathbf{V}_j) \oplus \mathbf{W}_j^2 . \tag{16}$$

Then, by inserting $\mathbf{V}_{j-1} = \mathbf{V}_j \oplus \mathbf{W}_j$ in equation (16), simple algebra yields:

$$\mathbf{W}_j^2 = (\mathbf{V}_j \otimes \mathbf{W}_j) \oplus (\mathbf{W}_j \otimes \mathbf{V}_j) \oplus (\mathbf{W}_j \otimes \mathbf{W}_j) . \tag{17}$$

As in the 1D case, the overall space $L^2(\mathbb{R}^2)$ can be decomposed as an orthogonal sum of the detail spaces at all resolutions [74–76]:

$$L^2(\mathbb{R}^2) = \oplus_{j=-\infty}^{+\infty} \mathbf{W}_j^2 . \tag{18}$$

A separable wavelet orthonormal basis of $L^2(\mathbb{R}^2)$ can thus be constructed with separable products of a scaling function ϕ and a wavelet ψ generating a wavelet orthogonal basis of $L^2(\mathbb{R})$. Let us define the following three wavelets [74–76]:

$$\begin{aligned}
\psi^1(x, y) &= \phi(x)\psi(y) , \\
\psi^2(x, y) &= \psi(x)\phi(y) , \\
\psi^3(x, y) &= \psi(x)\psi(y) ,
\end{aligned} \tag{19}$$

which take the following values on the 2D square grid:

$$\begin{aligned}
\psi_{j,m,n}^k(x, y) &= \\
&\frac{1}{2^j} \psi^k \left(\frac{x - 2^j(m + 1/2)}{2^j}, \frac{y - 2^j(n + 1/2)}{2^j} \right) ,
\end{aligned} \tag{20}$$

where $1 \leq k \leq 3$. According to equation (17), the wavelet family

$$\left\{ \psi_{j,m,n}^1(x, y), \psi_{j,m,n}^2(x, y), \psi_{j,m,n}^3(x, y) \right\}_{(m,n) \in \mathbb{Z}^2} \tag{21}$$

is an orthonormal basis of $\mathbf{W}_j^2$. From equation (18), one deduces that

$$\left\{ \psi_{j,m,n}^1(x, y), \psi_{j,m,n}^2(x, y), \psi_{j,m,n}^3(x, y) \right\}_{(j,m,n) \in \mathbb{Z}^3} \tag{22}$$

is an orthonormal basis of $L^2(\mathbb{R}^2)$.

The Fourier transform of the three separable wavelets [76] calculated from a 1D Daubechies 8 wavelet are shown in Figure 4. Wavelet coefficients calculated with ψ^1 and ψ^2 are large along edges which are respectively horizontal and vertical. The wavelet ψ^3 produces large coefficients at the corners. Note that the separable wavelet expressions (Eq. (19)) imply that $\hat{\psi}^1(k_x, k_y) = \hat{\phi}(k_x)\hat{\psi}(k_y)$, $\hat{\psi}^2(k_x, k_y) = \hat{\phi}(k_y)\hat{\psi}(k_x)$ and $\hat{\psi}^3(k_x, k_y) = \hat{\psi}(k_x)\hat{\psi}(k_y)$. Let us point out that in order to approach spatial isotropy, the respective weights on (ψ^1, ψ^2, ψ^3) have to be in the ratios $(1, 1, 1/2^{\tau(2)/4+1})$, at least on average.

2.2.2 Random $\mathcal{W}$-cascades

Let us consider the set $\{\psi^1_{j,m,n}, \psi^2_{j,m,n}, \psi^3_{j,m,n}\}$ of 2D separable compactly supported wavelets that form an orthonormal basis of L-periodic functions of $L^2_{\mathrm{per}}([0, L]^2)$, where $L = 2^N$. Thus $\forall f \in L^2_{\mathrm{per}}([0, L]^2)$, f can be written under the form:

$$f(\mathbf{x}) = \sum_{j=0}^{N} \sum_{m,n=0}^{2^{N-j}-1} \sum_{k=0}^{3} c^k_{j,m,n} \psi^k_{j,m,n}(\mathbf{x}) , \qquad (23)$$

where the set of coefficients $\{c^k_{j,m,n} = \langle \psi^k_{j,m,n}|f\rangle\}$ provides a complete characterization of the function f. The notion of cascade is then rather natural on the 2D square grid. The construction rule is very similar to the one used in 1D on wavelet dyadic trees [60–64]. We build a random function $f(\mathbf{x})$ by specifying its wavelet coefficients $\{c^k_{j,m,n}\}$ in a recursive way. Actually, it is the modulus

$$d_{j,m,n} = \left(\left[c^1_{j,m,n} \right]^2 + \left[c^2_{j,m,n} \right]^2 + \left[c^3_{j,m,n} \right]^2 \right)^{1/2} , \quad (24)$$

that one generates at successive scales, by iterating the following system:

$$d_{j-1,2m,2n} = M^{(r1)}_{j,m,n} d_{j,m,n} ,$$
$$d_{j-1,2m+1,2n} = M^{(r2)}_{j,m,n} d_{j,m,n} ,$$
$$d_{j-1,2m,2n+1} = M^{(r3)}_{j,m,n} d_{j,m,n} ,$$
$$d_{j-1,2m+1,2n+1} = M^{(r4)}_{j,m,n} d_{j,m,n} , \qquad (25)$$

for all j ($1 \leq j \leq N$), m ($0 \leq m < 2^{N-j}$) and n ($0 \leq n < 2^{N-j}$) and where the $M^{(ri)}_{j,m,n}$ are independent identically distributed (i.i.d.) positive valued random variables with prescribed law $P(M)$. To go from the $d_{j,m,n}$ modulus coefficients to the $c^k_{j,m,n}$ ($1 \leq k \leq 3$) wavelet coefficients, one has to specify the value of the angles (θ, φ) involved in the following expressions:

$$c^1_{j,m,n} = \cos(\varphi)\cos(\theta)d_{j,m,n} ,$$
$$c^2_{j,m,n} = \cos(\varphi)\sin(\theta)d_{j,m,n} ,$$
$$c^3_{j,m,n} = \sin(\varphi)d_{j,m,n} . \qquad (26)$$

where $\theta \in [-\pi, \pi]$ and $\varphi \in [-\pi/2, \pi/2]$.

To generate a given realization of the $\mathcal{W}$-cascade, one starts, at large scale, from arbitrarily chosen values of the coefficients $c^k_{N,0,0}$ ($1 \leq k \leq 3$), i.e., from an arbitrarily chosen value of $d_{N,0,0}$. Then one generates the coefficients $d_{j,m,n}$ at successive scales, by iterating equation (25). At each step and for each realization of the random variable M, the angle θ and φ in equation (26) are independently and randomly chosen with a white distribution on $[\theta_{min}, \theta_{max}]$ and $[\varphi_{min}, \varphi_{max}]$ respectively. Let us point out that the so-obtained random function $f(\mathbf{x})$ (assuming that the sum $\sum_{j=0}^{N}$ in equation (23), which actually should be an infinite sum $\sum_{j=-\infty}^{N}$, converges) is self-similar in the sense that the law of a wavelet coefficient $d_{j,m,n}$ at the scale 2^j can be linked to the law of another wavelet coefficient $d_{j',m',n'}$ at the scale $2^{j'} > 2^j$ using a multiplicative random variable depending only on the ratio of the two scales:

$$d_{j,m,n} \simeq_l d_{j',m,n} X_{j'-j} , \qquad (27)$$

where $\simeq_l$ stands for the equality in law and where $X_j = \prod_{i=1}^{N-j} M_i$ (the M_i's are i.i.d. positive valued random variables with the same law as M). Thus, from a statistical point of view, the details of the function f at a scale a are the same as the details at a scale a' up to a rescaling factor that depends only on a'/a.

Remark

Let us note that equation (25) can be rewritten as

$$\ln d_{j-1,2m,2n} = \ln d_{j,m,n} + \ln M^{(r1)}_{j,m,n} ,$$
$$\ln d_{j-1,2m+1,2n} = \ln d_{j,m,n} + \ln M^{(r2)}_{j,m,n} ,$$
$$\ln d_{j-1,2m,2n+1} = \ln d_{j,m,n} + \ln M^{(r3)}_{j,m,n} ,$$
$$\ln d_{j-1,2m+1,2n+1} = \ln d_{j,m,n} + \ln M^{(r4)}_{j,m,n} . \qquad (28)$$

If M is log-normal, these equations correspond to what one could call a tree-autoregressive process. This process is of order 1 in the sense that the regression involves only one term. We refer the reader to the work of Basseville and co-workers [102] for some introduction to autoregressive models lying on a tree (including the orthonormal wavelet dyadic tree). As previously emphasized in Ref. [64], our approach of $\mathcal{W}$-cascades in 1D as well as in 2D, is significantly different from theirs since we concentrate on the analysis of the fractal function f itself and not on the properties of the tree-process.

2.2.3 Numerical simulations of 2D $\mathcal{W}$-cascades

As inspired from the modeling of the energy cascading process in fully developed turbulence by log-infinitely divisible multiplicative processes [21–25,61–63], we will mainly concentrate here on the synthesis of multifractal rough surfaces using log-normal and log-Poisson $\mathcal{W}$-cascades.

Log-normal $\mathcal{W}$-cascades

Let us first start with M being a log-normal random variable. If m and σ^2 are, respectively, the mean and the variance of $\ln M$, then a straightforward computation leads to the following $\tau(q)$ spectrum:

$$\tau(q) = -\log_2\langle M^q\rangle - 2 \ , \ \forall q \in \mathbb{R}$$
$$= -\frac{\sigma^2}{2\ln 2}q^2 - \frac{m}{\ln 2}q - 2 \ , \tag{29}$$

where $\langle\ldots\rangle$ means ensemble average. The corresponding $D(h)$ singularity spectrum is obtained by Legendre transforming equation (29):

$$D(h) = -\frac{(h+m/\ln 2)^2}{2\sigma^2/\ln 2} + 2 \ . \tag{30}$$

According to the convergence criteria established in 1D [64], we will only consider parameter values that satisfy the conditions:

$$m < 0 \ \text{ and } \ \frac{|m|}{\sigma^2} > 2\sqrt{\ln 2} \ . \tag{31}$$

Moreover, by solving $D(h) = 0$, one gets $h_{\min}$ and $h_{\max}$:

$$h_{\min} = -\frac{m}{\ln 2} - \frac{2\sigma}{\sqrt{\ln 2}} \ ,$$
$$h_{\max} = -\frac{m}{\ln 2} + \frac{2\sigma}{\sqrt{\ln 2}}. \tag{32}$$

In Figure 5 are illustrated 3 realizations of a log-normal $\mathcal{W}$-cascade corresponding to 3 different ways of distributing the weights on ψ^1, ψ^2 and ψ^3 during the construction. The Fourier transforms of these 3 images are also shown in order to evidence some underlying anisotropy induced by the intrinsic anisotropy of the separable wavelets ψ^k ($1 \leq k \leq 3$). The model parameters are fixed to the values $m = -0.38\ln 2$ and $\sigma^2 = 0.03\ln 2$; 10 cascade steps have been used to generate these images.

(i) In Figure 5a, we start from the following wavelet coefficients at the largest scale:

$$c^1_{N,0,0} = 1 \ , \ c^2_{N,0,0} = 1 \ , \ c^3_{N,0,0} = 0 \ . \tag{33}$$

At each step of the cascade, the multiplier M is randomly chosen with the previously defined log-normal distribution. θ is randomly chosen between $[-\pi,\pi]$ while $\varphi = 0$ is kept fixed. This means that the so-generated $\mathcal{W}$-cascade develops on the wavelets ψ^1 and ψ^2 only. The corresponding Fourier transform in Figure 5b clearly displays anisotropic scaling with enhanced values along the k_x and k_y axis. This square lattice anisotropy results from the intrinsic anisotropic shape of ψ^1 and ψ^2.

(ii) In Figure 5c, the $\mathcal{W}$-cascade is generated on ψ^3 only. One starts at the largest scale from the following coefficients:

$$c^1_{N,0,0} = 0 \ , \ c^2_{N,0,0} = 0 \ , \ c^3_{N,0,0} = 1 \ , \tag{34}$$
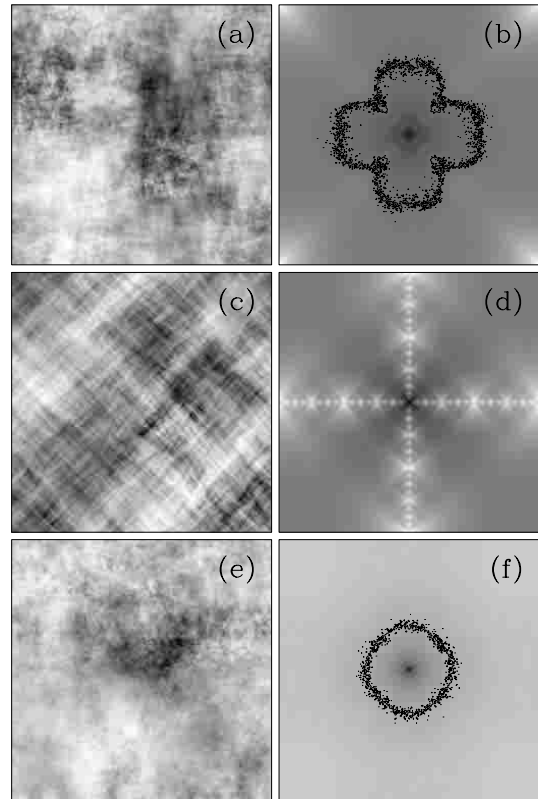
Fig. 5. Three realizations of a log-normal $\mathcal{W}$-cascade ($n = 10$) with parameter values $m = -0.38\ln 2$ and $\sigma^2 = 0.03\ln 2$, on separable orthonormal wavelets, using 1D "Daubechies 8" wavelet. (a) $\mathcal{W}$-cascade on ψ^1 and ψ^2 (case (i) in the text). (c) $\mathcal{W}$-cascade on ψ^3 (case (ii)). (e) $\mathcal{W}$-cascade on ψ^1, ψ^2 and ψ^3 (case (iii)). The corresponding Fourier transforms are shown in (b), (d), and (f) respectively. The fuzzy curves made of small black dots are level curves to guide the eyes. The amplitudes of f and $\hat{f}$ are coded using 32 grey levels from white (min f or min $\hat{f}$) to black (max f or max $\hat{f}$).

and during the cascading process, $\varphi = \pm\pi/2$ is chosen at random. As seen in the image of $f(\mathbf{x})$ itself, the particular shape of $\psi^3(x,y) = \psi(x)\psi(y)$ induces the presence of a texture with main axis along the diagonals. This anisotropy is clearly patent on the corresponding Fourier transform shown in Figure 5d.

(iii) In order to approach isotropy, one needs to adapt our strategy to the specificity of the $\mathcal{W}$-cascade one intends to generate. The specific shape of the analyzing wavelets ψ^1, ψ^2 and ψ^3 in Fourier space (Fig. 4), requires to adjust in a clever way the weights we put at each step on each of these wavelet modes. One starts at the largest scale from the following coefficients:

$$c^1_{N,0,0} = 1 \ , \ c^2_{N,0,0} = 1 \ , \ c^3_{N,0,0} = 2^{(-\tau(2)/4+1)} \ , \tag{35}$$

where $\tau(2) = \beta - 4$ is chosen according to the power-law decay of the energy spectrum one wants to impose. At each step, θ is randomly chosen between $[-\pi,\pi]$
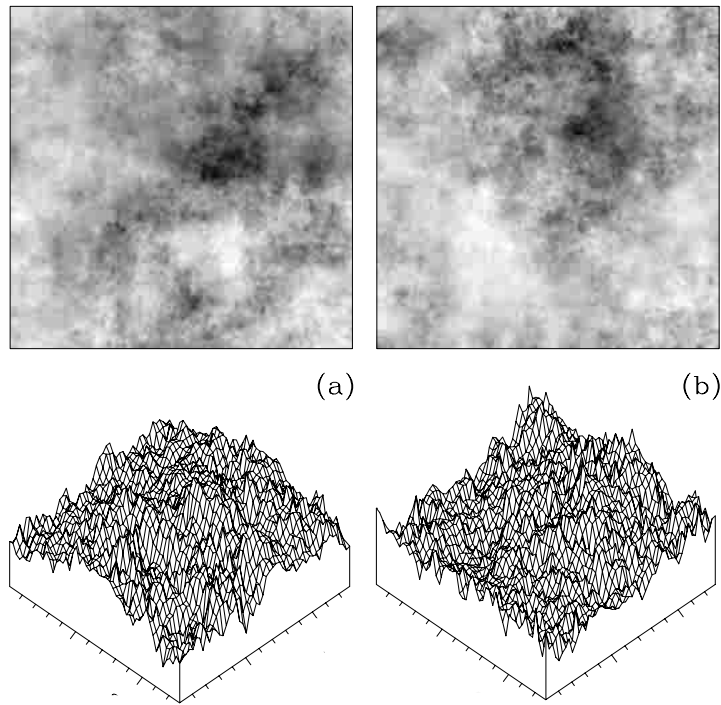
Fig. 6. Multifractal (1024×1024) rough surfaces generated using random $\mathcal{W}$-cascades ($n = 10$ steps). (a) Log-normal cascade with parameter values $m = -0.38 \ln 2$ and $\sigma^2 = 0.03 \ln 2$. (b) Log-Poisson cascade with the parameter values $\gamma = -1/9 \ln 2$, $\beta = (2/3)^{1/3}$ and $\lambda = 2 \ln 2$. Same coding as in Figure 5.

while the domain for φ needs to be adapted so that $\varphi \in [-\varphi^*, \varphi^*]$ (white distribution), where φ^* satisfies the following equation:

$$\frac{\sin 2\varphi^*}{4\varphi^*} = \frac{2^{\tau(2)/2+3}}{1 + 2^{\tau(2)/2+3}} - \frac{1}{2}, \ \varphi^* > 0. \quad (36)$$

The image shown in Figure 5e as well as its Fourier transform in Figure 5f, no longer display significant departure from isotropy. Even though each of the wavelets ψ^k ($1 \leq k \leq 3$) are clearly anisotropic, this does not prevent the synthesis of multifractal functions from approaching isotropic scaling properties (Note that there still remains some anisotropy coming from the underlying fragmentation process).

Figure 6a illustrates another realization of an "isotropic" log-normal $\mathcal{W}$-cascade together with the corresponding multifractal rough surface. The intermittent nature of $f(\mathbf{x})$ is enlightened on 1D cuts as shown in Figures 7a and 7b. From the power-spectrum power-law behavior in Figures 8a and 8b, one extracts a rather accurate estimate of the power-spectral exponent $\beta = \tau(2) + 4 = 2.70$, for the set of considered parameter values.

Fig. 7. 1D profiles obtained along some horizontal and vertical cuts in Figures 6a and 6b respectively. Log-normal $\mathcal{W}$-cascade: (a) horizontal profile; (b) vertical profile. Log-Poisson $\mathcal{W}$-cascade: (c) horizontal profile; (d) vertical profile.

Log-Poisson $\mathcal{W}$-cascades

Let λ be the mean and the variance of the Poisson distribution Y. We consider that the law of $\ln M$ is the same as $Y \ln \beta + \gamma$. A straightforward computation leads to the following $\tau(q)$ spectrum:

$$\tau(q) = \frac{\lambda(1 - \beta^q) - \gamma q}{\ln 2} - 2. \quad (37)$$
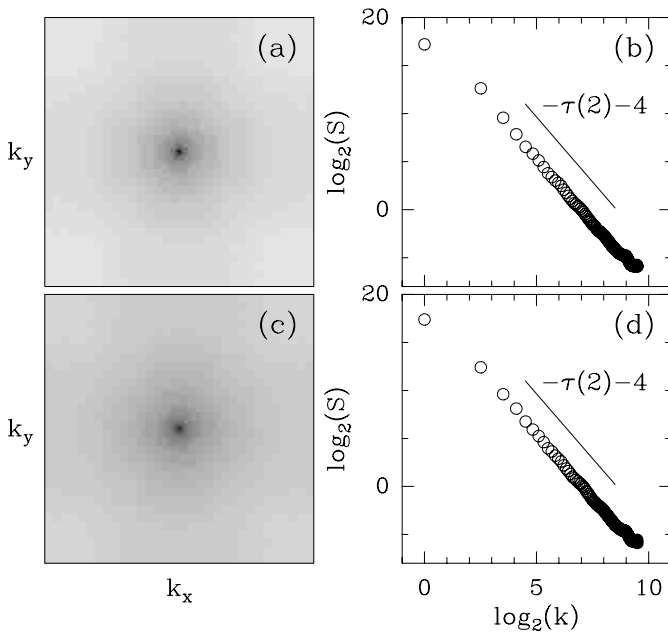
Fig. 8. Power-spectrum analysis of the (1024 × 1024) images shown in Figures 6a and 6b respectively. Log-normal $\mathcal{W}$-cascade: (a) $\ln|\hat{f}_{n=10}(\mathbf{k})|$; (b) $S(|\mathbf{k}|)$ *vs.* $|\mathbf{k}|$ in logarithmic representation. Log-Poisson $\mathcal{W}$-cascade: (c) $\ln|\hat{f}_{n=10}(\mathbf{k})|$; (d) $S(|\mathbf{k}|)$ *vs.* $|\mathbf{k}|$ in logarithmic representation. The solid lines in (b) and (d) correspond to the theoretical power-law prediction with exponent $\beta = \tau(2) + 4 = 2.70$.

The corresponding $D(h)$ singularity spectrum obtained by Legendre transforming $\tau(q)$ writes:

$$D(h) = \left(\frac{h}{\ln\beta} + \frac{\gamma}{\ln 2 \ln\beta} \right) \left(\ln \left(\frac{h + \gamma/\ln 2}{-(\lambda/\ln 2)\ln\beta} \right) - 1 \right)$$
$$- \frac{\lambda}{\ln 2} + 2 . \quad (38)$$

Very much like the spectra obtained for log-normal $\mathcal{W}$-cascades, $\tau(q)$ is a nonlinear function of q while $D(h)$ has a single humped shape characteristic of multifractal scaling properties.

In Figure 6b is shown a multifractal rough surface generated with the log-Poisson $\mathcal{W}$-cascade model with parameter values $\gamma = -1/9 \ln 2$, $\beta = (2/3)^{1/3}$ and $\lambda = 2\ln 2$. 1D profiles obtained along horizontal and vertical 1D cuts are illustrated in Figures 7c and 7d. From a qualitative point of view, this rough surface looks intermittent very much like the one obtained with a log-normal $\mathcal{W}$-cascade. Actually, as seen on the power-spectrum analysis in Figures 8c and 8d, the numerical data are in good agreement with the theoretical prediction for the spectral exponent $\beta = \tau(2) + 4 = 2.70$. Let us remark that because of our specific choices for the model parameter values, both the log-normal and log-Poisson $\mathcal{W}$-cascades generate multifractal rough surfaces with the same $\tau(2)$ exponent and in turn the same spectral exponent β. From a quantitative point of view, the data in Figures 8c and 8d fail to distinguish log-Poisson from log-normal $\mathcal{W}$-cascades. This

observation is not so surprising since we already know that power spectrum analysis fails to discriminate between rough surfaces that display multifractal scaling properties from those which are homogeneous and monofractal. In particular, a fractional Brownian surface $B_H(\mathbf{x})$ with the index $H = (\tau(2) + 2)/2 = 0.35$, displays the same power-law decay than the power spectra in Figures 8b and 8d (see Sect. 5 in paper I [68]).

Remark

As previously discussed for 1D random $\mathcal{W}$-cascades in reference [64], there is no reason, *a priori*, that all the realizations of the same stochastic multifractal functions correspond to a unique $D(h)$-curve. Each realization has its own unique distribution of singularities and the crucial issue is to relate the theoretical singularity spectrum defined by equation (58) in paper I [68] to the statistical $D(h)$ spectrum given by equations (30) and (38) respectively. From the mathematical results proved for 1D random $\mathcal{W}$-cascades [64], the statistical $D(h)$ spectrum obtained with the multifractal WTMM formalism, is likely to be an upper bound for the theoretical singularity spectrum (at least for its left increasing branch).

3 WTMM analysis of synthetic multifractal rough surfaces

This section is devoted to the application of the 2D WTMM method to synthetic multifractal rough surfaces generated with the two classes of models described in Section 2. We systematically follow the numerical implementation procedure described in Section 4.3 of paper I [68]. For each model, we first wavelet transform 32 (1024 × 1024) images of the stochastic multifractal rough surfaces with an isotropic first-order analyzing wavelet. To master edge effects, we then restrain our analysis to the (512 × 512) central part of the wavelet transform of each image. From the wavelet transform skeleton defined by the WTMMM, we compute partition functions from which we extract the $\tau(q)$ and $D(h)$ multifractal spectra (Sect. 4.2 of paper I [68]). We systematically test the robustness of our estimates with respect to some change in the shape of the analyzing wavelet, in particular when increasing the number of zero moments.

3.1 Multifractal rough surfaces generated by the fractionally integrated singular cascade model

In Figure 9 is illustrated the computation of the maxima chains and the WTMMM for an individual image of a random multifractal rough surface generated with the fractionally integrated singular cascade model described in Section 2.1 [72,99–101], for the following parameter values: $p = 0.32$ and $H^* = 0.638$ (Fig. 1b). In Figure 9b is
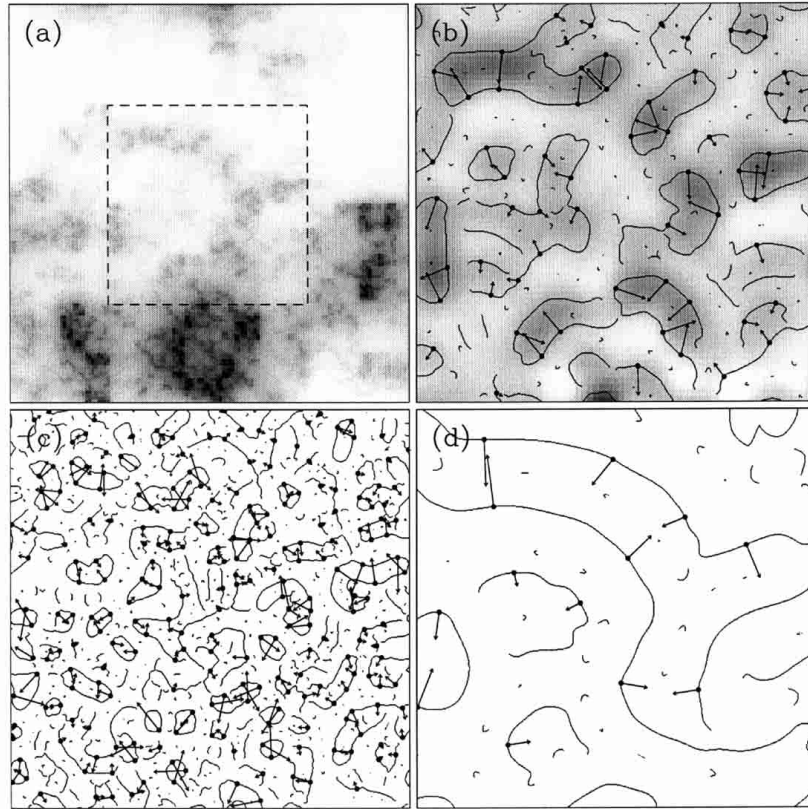
Fig. 9. 2D wavelet transform analysis of a multifractal rough surface generated with the fractionally integrated singular cascade model ($p = 0.32$, $H^* = 0.638$). ψ is a third-order radially symmetric analyzing wavelet (see Fig. 1 of paper I [68]). (a) 32 grey-scale coding of the original (1024×1024) image. In (b) $a = 2^{2.9}\sigma_W$, (c) $a = 2^{1.9}\sigma_W$ and (d) $a = 2^{3.9}\sigma_W$ (where $\sigma_W = 13$ pixels), are shown the maxima chains; the local maxima of $\mathcal{M}_\psi$ along these chains are indicated by ($\bullet$) from which originates an arrow whose length is proportional to $\mathcal{M}_\psi$ and its direction (with respect to the x-axis) is given by $\mathcal{A}_\psi$; only the (512×512) central part delimited by a dashed square in the original image in (a) is taken into account to define the WT skeleton. In (b), the smoothed image $\phi_{\mathbf{b},a} * f$ is shown as a grey-scale coded background from white (min) to black (max).

shown the convolution of the original image (Fig. 9a) with the isotropic mexican hat smoothing filter ϕ. According to the definition of the WTMM, the maxima chains correspond to well defined edge curves of the smoothed image. The local maxima of $\mathcal{M}_\psi$ along these curves are indicated by ($\bullet$) from which originates an arrow whose length is proportional to $\mathcal{M}_\psi$ and its direction (with respect to the x-axis) is given by $\mathcal{A}_\psi$. After linking these WTMMM across scales, one constructs the WT skeleton from which one computes the partition functions $\mathcal{Z}(q, a)$ (Eq. (59) of paper I [68]). As reported in Figure 10a, the annealed average partition functions display a well defined scaling behavior over about 4 octaves when plotted *versus a* in a logarithmic representation. When processing to a linear regression fit of the data over the first four octaves, one gets the $\tau(q)$ spectrum shown in Figure 10c. In contrast to fractional Brownian rough surfaces studied in Section 5 of paper I [68], this $\tau(q)$ spectrum unambiguously deviates from a straight line. Moreover, for $-4 \leq q \leq 9$, the data are in remarkable agreement with the theoretical spectrum given in equation (8). The values of

$h = \partial\tau/\partial q$ range in the interval $\sim [0.18, 1.30]$, which means that $h_{\max} > 1$, *i.e.*, the multifractal function under study has singularities in its first derivative also. This result is corroborated by the scaling behavior of the expectation value $h(q, a)$, defined in equation (66) in paper I [68], which clearly depends on q in Figure 10b. When Legendre transforming the nonlinear $\tau(q)$ spectrum obtained in Figure 10c, one gets the $D(h)$ singularity spectrum reported in Figure 10d. Its characteristic single humped shape over a finite range of Hölder exponents is a clear signature of the multifractal nature of the synthetic rough surfaces generated by the fractionally integrated singular cascade model. For $q = 0$, the largest dimension is attained for singularities of Hölder exponent $h(q = 0) = 0.74 \pm 0.02$, a value which is in good agreement with the theoretical prediction $h(q = 0) = 0.738$. Moreover, the corresponding maximum of the $D(h)$ curve, $D(h(q = 0)) = -\tau(0) = 2.00 \pm 0.02$ does not deviate substantially from the theoretical value $D_F = 2$, which confirms that the considered random multifractal functions are singular everywhere.
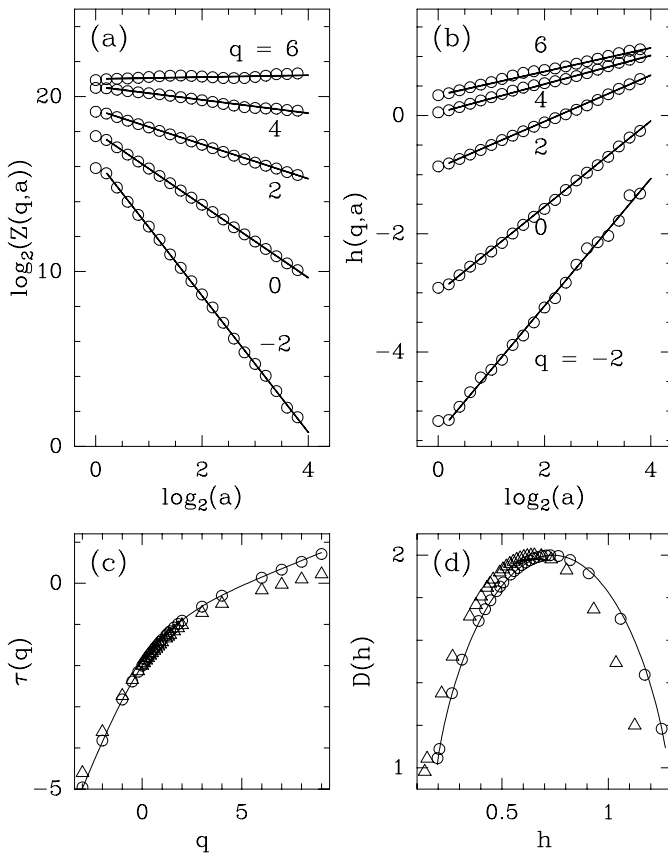
Fig. 10. Determination of the $\tau(q)$ and $D(h)$ spectra of multifractal rough surfaces generated with the fractionally integrated singular cascade model ($p = 0.32$, $H^* = 0.638$). The 2D WTMM method is used with a third-order radially isotropic analyzing wavelet ($\circ$). (a) $\log_2 \mathcal{Z}(q, a)$ vs. $\log_2 a$; the solid lines correspond to linear regression fit of the data over the first 4 octaves. (b) $h(q, a)$ vs. $\log_2 a$; the solid lines correspond to linear regression fit estimates of $h(q)$. (c) $\tau(q)$ vs. q as obtained from linear regression fit of the data in (a) over the first four octaves. (d) $D(h)$ vs. h, after Legendre transforming the $\tau(q)$ curve in (c). In (c) and (d), the symbols ($\triangle$) represent the results obtained when using a first-order radially symmetric analyzing wavelet. The solid lines correspond to the theoretical $\tau(q)$ (Eq. (8)) and $D(h)$ spectra. These results come from annealed averaging over 32 (1024×1024) images. a is expressed in σ_W units.

In Figures 10c and 10d are also shown for comparison the results obtained when applying the 2D WTMM method with a first-order analyzing wavelet (the smoothing function ϕ being a Gaussian). With our statistical sample of 32 (1024×1024) images, it is clear that the estimates of the $\tau(q)$ and $D(h)$ spectra are poorer than the results previously obtained with a third-order isotropic analyzing wavelet. This observation is a direct consequence of the fact that first-order analyzing wavelets are not adapted to characterize the fluctuations of multifractal functions whose singularity spectrum support extends beyond 1 ($h_{max} > 1$, *i.e.*, the weakest singularities are located in the first derivative of $f(\mathbf{x})$) on one side ($q < 0$), meanwhile it reaches almost 0 on the other side ($q > 0$). Ad-
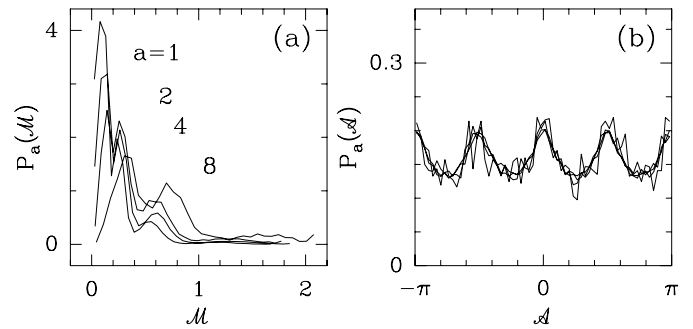
Fig. 11. Pdf's of the WTMMM coefficients of synthetic multifractal rough surfaces generated with the fractionally integrated singular cascade model ($p = 0.32$, $H^* = 0.638$). (a) $P_a(\mathcal{M})$ vs. $\mathcal{M}$. (b) $P_a(\mathcal{A})$ vs. $\mathcal{A}$. ψ is a third-order radially symmetric analyzing wavelet. Four different scales $a = 1, 2, 4, 8$ (in σ_W units) are shown. These results correspond to averaging over 32 (1024×1024) images.
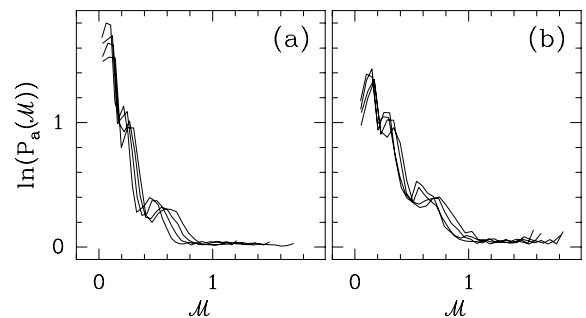
Fig. 12. Pdf's of $\mathcal{M}$ when conditioned by $\mathcal{A}$. The different curves correspond to fixing $\mathcal{A}$ (mod π) to $0 \pm \pi/8$, $\pi/4 \pm \pi/8$, $\pi/2 \pm \pi/8$ and $3\pi/4 \pm \pi/8$. (a) $a = 2^{0.1}$; (b) $a = 2^{1.1}$ (in σ_W units). Same 2D WTMM computations as in Figure 11.

ditional computations on 32 newly generated images improve the agreement with the theoretical $\tau(q)$ spectrum. For the class of multifractal rough surfaces studied in this section, it is clear that the use of a third-order analyzing wavelet allows us to master in a more efficient way the problem of the fractional integration to the benefit of a better characterization of the multiplicative nature of the underlying singular cascade.

In Figure 11 are shown the corresponding pdfs $P_a(\mathcal{M}) = \int d\mathcal{A} \, P_a(\mathcal{M}, \mathcal{A})$ and $P_a(\mathcal{A}) = \int d\mathcal{M} \, P_a(\mathcal{M}, \mathcal{A})$, for four different values of the scale parameter a.

As seen in Figure 11a, whatever the value of a, $P_a(\mathcal{M})$ displays some oscillatory decreasing tail as the signature of the underlying discrete multiplicative process (prior to the fractional integration). Note that the main peaks observed in these distributions occur for values of $\mathcal{M}$ within a proportional ratio very close to $(1 - p)/p = 0.68/0.32 = 2.125$. In Figure 11b, $P_a(\mathcal{A})$ clearly does not evolve across scales, which means that the scale invariance properties of the considered synthetic rough surfaces are contained in the scale dependence of the $\mathcal{M}$-pdf. However, some oscillatory departure from a flat distribution is observed with
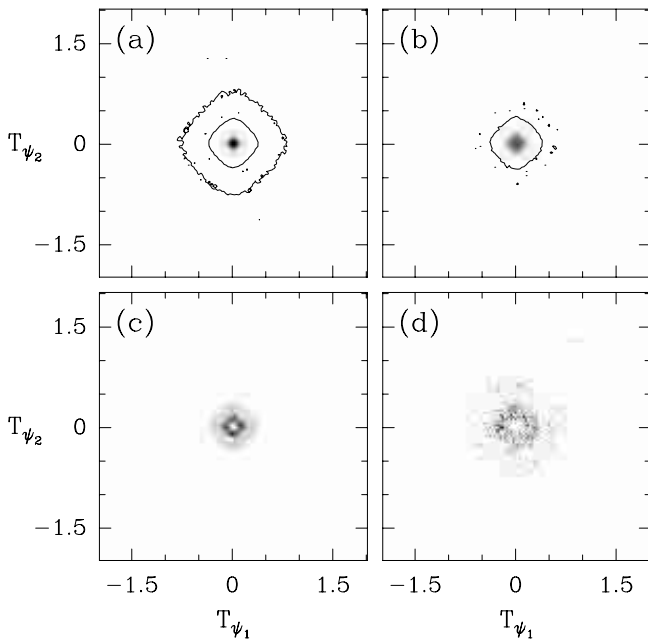
Fig. 13. Distribution of the WTMMM in the plane (T_{ψ_1}, T_{ψ_2}) for the following values of the scale parameter: $a = 1$ (a), 2 (b), 4 (c) and 8 (d) in σ_W units. Same 2D WTMM computations as in Figure 11.

Fig. 14. Pdf's of $\mathcal{M}$ as computed at different scales $a = 1$, 2, 4 and 8 (in σ_W units). (a) $\ln P_a(\mathcal{M})$ *vs.* $\mathcal{M}$. (b) $\ln P_a(\mathcal{M})$ *vs.* $\mathcal{M}/a^{h(q=0)}$ with $h(q = 0) = 0.738$. Same 2D WTMM computations as in Figure 11.

well defined maxima for $\mathcal{A} = 0$, $\pi/2$, π and $3\pi/2$. This anisotropy in the reconstructed images (Fig. 1b) is the direct consequence of the privileged role played by the x- and y-axis in the binomial cascade process prior to the fractional integration. Hopefully, this anisotropy does not disturb the scaling properties of $\mathcal{M}$ since, as reported in Figure 12 for two different scales, the pdf of $\mathcal{M}$, when conditioned by the argument $\mathcal{A}$, is shown to be shape invariant. This independence of $\mathcal{M}$ and $\mathcal{A}$ is further illustrated in Figure 13 where the WTMMM are plotted in the (T_{ψ_1}, T_{ψ_2}) plane (see Sect. 2 of paper I [68]). For the 4 scales represented, the distributions so obtained are clearly "square" symmetric as the signature of the factorization of the joint probability distribution: $P_a(\mathcal{M}, \mathcal{A}) = P_a(\mathbb{F}(\mathcal{A})\mathcal{M})P_a(\mathcal{A})$, where $\mathbb{F}(\mathcal{A})$ is a function that does not depend on the scale parameter and that allows us to superimpose perfectly the curves in Figures 12a and 12b ($\mathbb{F}(\mathcal{A})$ accounts simply for this square anisotropy but does not affect the scaling properties of the partition functions); $P_a(\mathcal{A})$ is the scale independent distribution found in Figure 11b.

All the multifractal properties of the rough surfaces generated by the fractionally integrated singular cascade model are thus contained in the way the shape of the pdf of $\mathcal{M}$ evolves when one decreases the scale parameter a. This evolution is illustrated in Figure 14a when using a semilogarithmic representation. As experienced in paper I [68] for fractional Brownian surfaces, a test of monofractal self-similar scaling is the existence of a unique exponent h which allows us to rescale all the pdf's $P_a(\mathcal{M})$ computed at different scales, onto a universal function $\mathbb{P}$ independent

of a, and which satisfies:

$$P\Big(\mathcal{M}_{\boldsymbol{\psi}}\big(\mathcal{L}(a)\big)\Big) = \mathbb{P}\Big(\mathcal{M}_{\boldsymbol{\psi}}\big(\mathcal{L}(a)\big)/a^h\Big) . \tag{39}$$

In Figure 14b, we have tried to find such an exponent without any success. The results reported in this figure correspond to rescaling the WTMMM by $a^{h(q=0)}$, where $h(q = 0) = \lim_{a \to 0^+} h(q = 0, a)/\ln a$ (Eq. (68) in paper I [68]) $= \partial\tau/\partial q|_{q=0}$, is the Hölder exponent which is the most frequently encountered in the rough surfaces under consideration. As compared to the remarkable collapse obtained in Figure 27 of paper I for $B_{1/3}(\mathbf{x})$, the pdf's obtained after rescaling in Figure 14b are clearly different. Equation (39) is thus absolutely not relevant for those synthetic rough surfaces whose intermittent fluctuations display multifractal scaling properties as characterized by a singularity spectrum which involves a continuum of (Hölder) scaling exponents (Fig. 10d).

3.2 Multifractal rough surfaces generated by random cascades on separable wavelet orthogonal basis

This section is devoted to the application of the 2D WTMM method to multifractal functions synthetized from $\mathcal{W}$-cascades on separable wavelet orthogonal basis as defined in Section 2.2. We mainly report results obtained with the first-order radially symmetric analyzing wavelets shown in Figure 1 of paper I [68]. Possibly because of the range of Hölder exponent values which is restricted to $h \in [0, 1]$, but more probably because of the underlying multiplicative structure of the multifractal surface itself (without any need of some power-law filtering), a first-order analyzing wavelets leads to numerical multifractal spectra which are in remarkable agreement with the theoretical predictions. Let us point out that quite robust results are obtained with the third-order analyzing wavelet used in the previous sub-section.
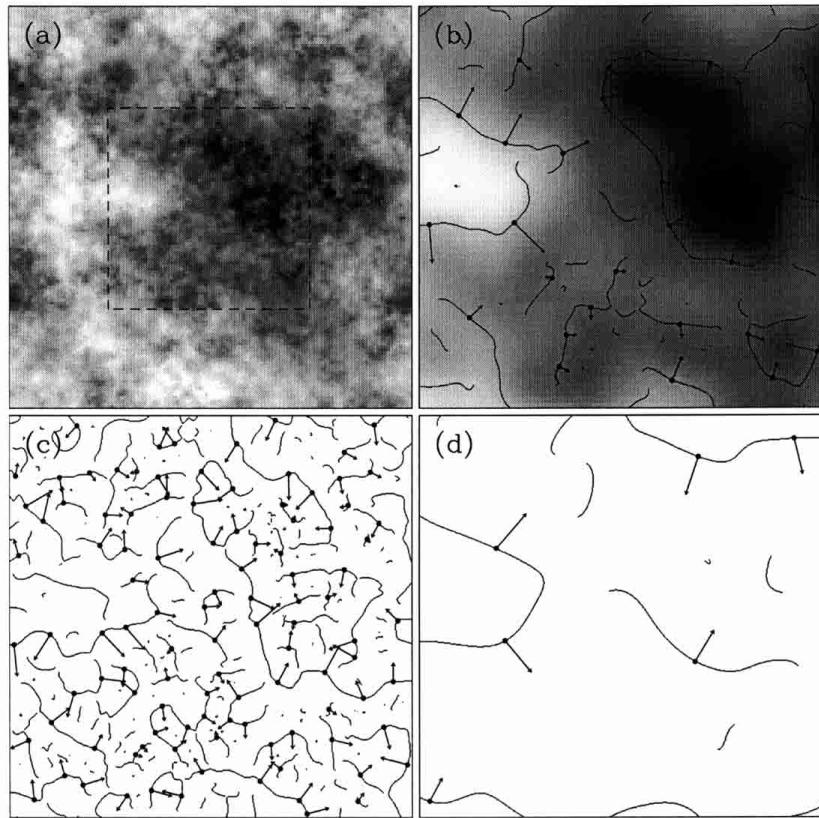
Fig. 15. 2D wavelet transform analysis of a multifractal rough surface generated with the log-normal $\mathcal{W}$-cascade model. Same model parameters as in Figure 6a. ψ is the first-order radially symmetric analyzing wavelet shown in Figure 1 of paper I [68]. (a) 32 grey-scale coding of the original (1024 × 1024) image. In (b) $a = 2^{2.9}\sigma_W$, (c) $a = 2^{1.9}\sigma_W$ and (d) $a = 2^{3.9}\sigma_W$, are shown the maxima chains and the WTMMM for the central (512 × 512) part of the original image (dashed square in (a)). In (b), the smoothed image $\phi_{\mathbf{b},a} * f$ is shown as a grey-scale coded background from white (min) to black (max).

3.2.1 Log-normal $\mathcal{W}$-cascades

In Figure 15 is illustrated the computation of the maxima chains and the WTMMM for an individual image of a multifractal rough surface generated with the log-normal $\mathcal{W}$-cascade model described in Section 2.2. The model parameters are the same as the ones used in Figure 6a, namely $m = -0.38 \ln 2$ and $\sigma^2 = 0.03 \ln 2$. Equations (35, 36) are implemented in order to approach as much as possible isotropic scaling. Again Figure 15b illustrates perfectly the fact that the maxima chains correspond to edge curves of the original image after smoothing by a Gaussian filter ϕ. From the WTMMM defined on these maxima chains, one constructs the WT skeleton according to the procedure described in Section 4 of paper I [68]. From the WT skeletons of 32 (1024 × 1024) images like the one in Figure 15a, one computes the annealed average of the partition functions $\mathcal{Z}(q,a)$. As shown in Figure 16a, when plotted *versus* the scale parameter a in a logarithmic representation, these annealed average partition functions display a rather impressive scaling behavior over a range of scales of about 4 octaves (*i.e.*, $\sigma_W \lesssim a \lesssim 16\sigma_W$, where $\sigma_W = 13$ pixels). Let us point out that scal-

ing of quite good quality is found for a rather wide range of values of q: $-6 \lesssim q \lesssim 8$. When processing to a linear regression fit of the data over the first four octaves, one gets the $\tau(q)$ spectrum ($\circ$) shown in Figure 16c. For the range of q values where scaling is operating, the numerical data are in remarkable agreement with the theoretical nonlinear $\tau(q)$ spectrum given by equation (29). Similar quantitative agreement is observed on the $D(h)$ singularity spectrum in Figure 16d. Let us note that consistant parabolic shapes are obtained when using either the Legendre transform of the $\tau(q)$ data or the formula (68) and (69) of paper I [68] to compute $h(q)$ and $D(q)$. In Figure 16b are reported the results for the expectation values $h(q,a)$ (Eq. (66) of paper I [68]) *vs.* $\log_2 a$; it is clear on this figure that the slope $h(q)$ depends upon q, the hallmark of multifractal scaling. Note that again, the theoretical predictions $h(q) = \partial\tau/\partial q = -\sigma^2 q/\ln 2 - m/\ln 2$ provide very satisfactory fits of the numerical data. From equation (32), the multifractal rough surfaces under study, display intermittent fluctuations corresponding to Hölder exponent values ranging from $h_{\min} = 0.034$ to $h_{\max} = 0.726$. Unfortunately, to capture the strongest and weakest singularities, one needs to compute the $\tau(q)$ spectrum for very large values of $|q|$. This requires the processing of many more
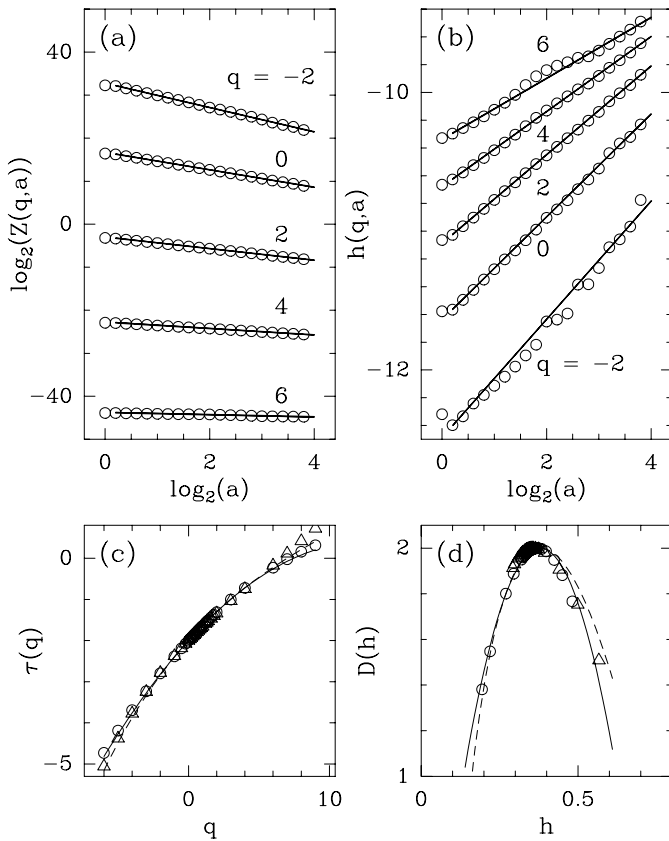
Fig. 16. Determination of the $\tau(q)$ and $D(h)$ spectra of multifractal rough surfaces generated with the log-normal ($\circ$) and log-Poisson ($\triangle$) random $\mathcal{W}$-cascade models, using the 2D WTMM method. ψ is the first-order radially symmetric analyzing wavelet used in Section 3.1. (a) $\log_2 \mathcal{Z}(q,a)$ *vs.* $\log_2 a$; the solid lines correspond to linear regression fit of the data over the first four octaves. (b) $h(q,a)$ *vs.* $\log_2 a$; the solid lines correspond to linear regression fit estimates of $h(q)$. (c) $\tau(q)$ *vs.* q as obtained from linear regression fit of the data in (a) over the first four octaves. (d) $D(h)$ *vs.* h, after Legendre transforming the $\tau(q)$ curve in (c). In (c) and (d), the solid lines represent the theoretical log-normal spectra (Eqs. (29, 30)); the log-Poisson predictions (Eqs. (37, 38)) are represented by the dashed lines.

images of much larger size, which is out of our current computer capabilities. Note that with the statistical sample studied here, one has $D(h(q=0)=0.38)=2.00\pm0.02$, which allows us to conclude that the rough surfaces under consideration are singular everywhere.

From the construction rule of these synthetic log-normal rough surfaces (Sect. 2.2.2), the multifractal nature of these random functions is expected to be contained in the way the shape of the WT modulus pdf $P_a(\mathcal{M})$ evolves when varying the scale parameter a, as shown in Figure 17a. Indeed the joint probability distribution $P_a(\mathcal{M},\mathcal{A})$ is expected to factorize, as the signature of the implicit decoupling of $\mathcal{M}$ and $\mathcal{A}$ in the construction process. This decoupling is numerically retrieved in Figure 18 where, for two different scales, the pdf of $\mathcal{M}$, when conditioned by the argument $\mathcal{A}$, is shown to be shape invari-
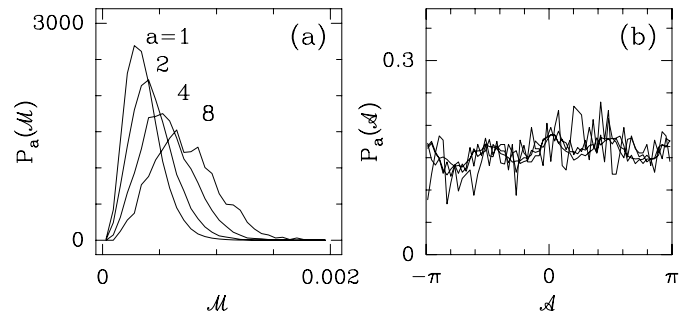
Fig. 17. Pdf's of the WTMMM coefficients of synthetic multifractal rough surfaces generated with the log-normal $\mathcal{W}$-cascade model ($m = -0.38\ln 2$ and $\sigma^2 = 0.03\ln 2$). (a) $P_a(\mathcal{M})$ vs $\mathcal{M}$. (b) $P_a(\mathcal{A})$ *vs.* $\mathcal{A}$. ψ is a first-order radially symmetric analyzing wavelet. Four different scales $a = 1, 2, 4, 8$ (in σ_W units) are shown. These results correspond to averaging over 32 (1024×1024) images.
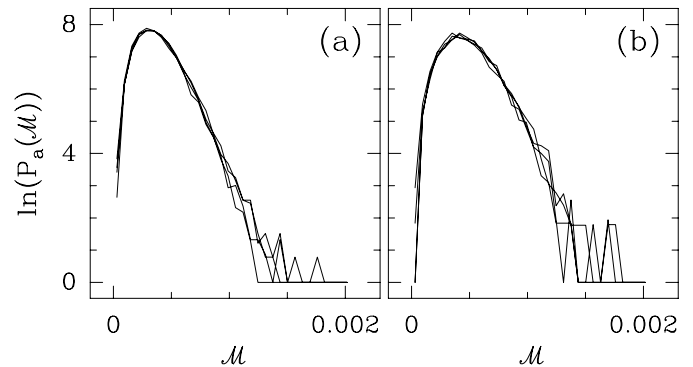
Fig. 18. Pdf's of $\mathcal{M}$ when conditioned by $\mathcal{A}$. The different curves correspond to fixing $\mathcal{A}$ (mod π) to $0 \pm \pi/8$, $\pi/4 \pm \pi/8$, $\pi/2 \pm \pi/8$ and $3\pi/4 \pm \pi/8$. (a) $a = 2^{0.1}$; (b) $a = 2^{1.1}$ (in σ_W units). Same 2D WTMM computations as in Figure 17.

ant. For further evidence of this statistical independence between $\mathcal{M}$ and $\mathcal{A}$, we refer the reader to Figure 19 where the WTMMM are plotted in the (T_{ψ_1}, T_{ψ_2}) plane. When varying the scale parameter a, no significant angular dependent evolution is observed in the distribution of the WTMMM. As seen in Figure 17b, $P_a(\mathcal{A})$ does not exhibit any significant change when increasing a, except some loss in regularity at large scales due to the rarefaction of the maxima lines. Let us point out that, even though $P_a(\mathcal{A})$ looks globally rather flat, one can notice some small amplitude almost periodic oscillations at the smallest scales which reflects the existence of privileged directions in the wavelet cascading process. These oscillations are maximum for $\mathcal{A} = 0, \pi/2, \pi$ and $3\pi/2$, as the witness to the square lattice anisotropy underlying the 2D wavelet tree decomposition.

Another way to evidence multifractality is to report the failure of the self-similarity relationship (39). As experienced in Figure 14b for the fractionally integrated singular cascades, we have tried to find a value of h such that, when rescaling the WTMMM by a^h, all the pdf $P_a(\mathcal{M})$ shown in Figure 20a in a semi-logarithmic representation, collapse onto a single curve. Clearly, we have not been able
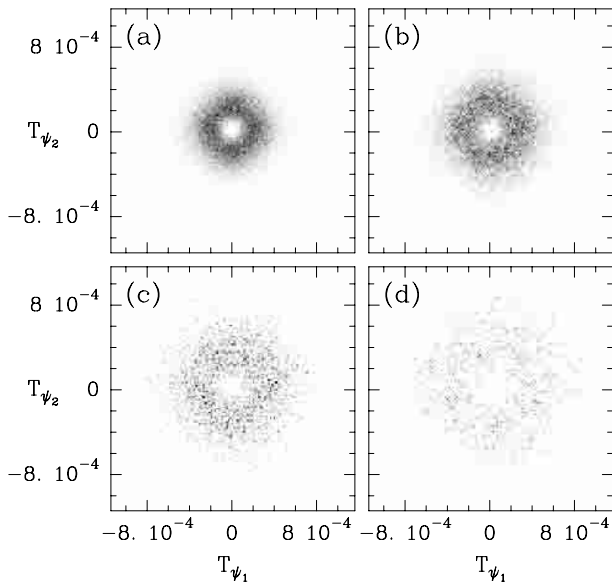
Fig. 19. Distribution of the WTMMM in the plane (T_{ψ_1}, T_{ψ_2}) for the following values of the scale parameter: $a = 1$ (a), 2 (b), 4 (c) and 8 (d) in σ_W units. Same 2D WTMM computations as in Figure 17.
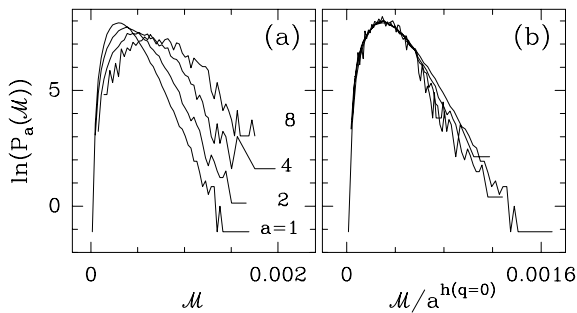
Fig. 20. Pdf's of $\mathcal{M}$ as computed at different scales $a = 1$, 2, 4 and 8 (in σ_W units). (a) $\ln P_a(\mathcal{M})$ *vs.* $\mathcal{M}$. (b) $\ln P_a(\mathcal{M})$ *vs.* $\mathcal{M}/a^{h(q=0)}$ with $h(q=0) = 0.38$. Same 2D WTMM computations as in Figure 17.

to find such a remarkable exponent. As reported in Figure 20b, when using the expected most frequent Hölder exponent $h(q = 0) = \partial\tau/\partial q|_{q=0} = -m/\ln 2 = 0.38$, the right tail of $P_a(\mathcal{M})$ shrinks to smaller values of $\mathcal{M}/a^h$ when a is increased. Although this evolution does not look very spectacular, its clearly deviates from the perfect collapse found for fBm surfaces in Figure 27b of paper I, the hallmark of monofractal scaling properties.

3.2.2 Log-Poisson $\mathcal{W}$-cascades

We have reproduced our 2D WTMM statistical analysis on 32 (1024×1024) images of multifractal rough surfaces generated with the log-Poisson $\mathcal{W}$-cascade model described in Section 2.2.2, with the parameter values $\gamma = -1/9 \ln 2$, $\beta = (2/3)^{1/3}$ and $\lambda = 2 \ln 2$. The results so obtained are

of the same good quality as those reported before for log-normal $\mathcal{W}$-cascades. As shown in Figures 16c and 16d, the $\tau(q)$ and $D(h)$ spectra obtained with the log-Poisson $\mathcal{W}$-cascades ($\triangle$) are found in remarkable agreement with the corresponding theoretical spectra (- - -) for values of q in the range $-6 \lesssim q \lesssim 8$, where well-defined scaling is observed. Let us remark that in this range of q values, for the considered sets of parameter values (which for both log-normal and log-Poisson $\mathcal{W}$-cascades are directly inspired from the multifractal 1D WTMM analysis of the longitudinal velocity fluctuations in fully developed turbulent flows [25,63,81]), the theoretical $\tau(q)$ spectrum given by equation (37) is almost undistinguishable from the theoretical $\tau(q)$ spectrum for the log-normal $\mathcal{W}$-cascades (29). It is therefore not surprising that our numerical analysis fails to distinguish log-Poisson from log-normal multifractal rough surfaces with the available statistical sample of synthetic (1024×1024) images. As seen in Figures 16c and 16d, the log-normal and log-Poisson theoretical multifractal spectra start departing one from the other at large $(q \gtrsim 6)$ and small $(q \lesssim -4)$ q values. Our numerical data also start separating one from each other at those rather large values of $|q|$ in a way which is quite consistent with the theoretical predictions. However, let us emphasize that, as previously discussed in paper I [68], finite-size effects as well as some lack of statistical convergence start affecting our estimates of the $\tau(q)$ exponents (and in turn the $D(h)$ singularity spectrum) which are no longer as reliable as they should be. This observation must not be considered as some limitation of the 2D WTMM method to discriminating between log-normal and log-Poisson statistic since, with other choices of parameter values, this discrimination can be shown to be quite operational. Because of the specific choice of the model parameters, the above observation simply indicates that in order to distinguish log-Poisson multifractal spectra from their log-normal approximations (see the discussion in Sect. 4), one needs to be able to investigate values of $|q| \gtrsim 6$ which requires many more images of much larger size than those investigated in the present study.

In Figures 21, 22 and 23, we report the results of the computation of the joint probability distribution $P_a(\mathcal{M}, \mathcal{A}) = P_a(\mathcal{M})P_a(\mathcal{A})$, which is found to factorize as previously observed for log-normal $\mathcal{W}$-cascades. These figures have to be compared with Figures 17, 18 and 19 discussed just above. The similarities between those two sets of data confirm the conclusions derived from the multifractal spectra computations. In Figure 24, one witnesses the impossibility of finding a value of the exponent h such that, when rescaling $\mathcal{M}$ by a^h, all the pdf's computed at different scales collapse onto a single curve. When using the most frequent Hölder exponent $h = h(q=0) = -(\gamma/\ln 2 + \lambda \ln \beta/\ln 2) = 0.381$ (a value which, up to 10^{-3}, is the same as for the log-normal $\mathcal{W}$-cascades in Fig. 20), the right tails of these pdf's fail to superimpose one on the top of each other. This discrepancy is the signature of multiscaling, *i.e.*, the existence of a continuum of scaling exponent values which account for the roughness fluctuations of the multifractal surfaces
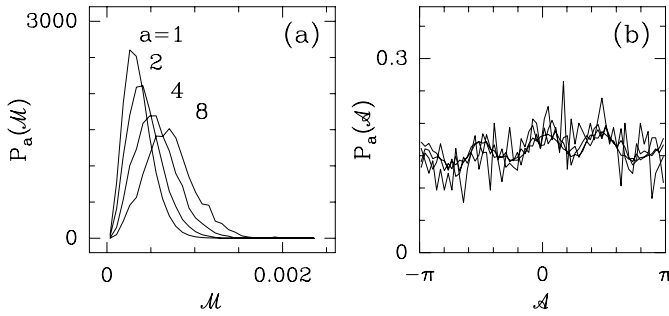
Fig. 21. Pdf's of the WTMMM coefficients of synthetic multifractal rough surfaces generated with the log-Poisson $\mathcal{W}$-cascade model ($\gamma = -1/9 \ln 2$, $\beta = (2/3)^{1/3}$ and $\lambda = 2\ln 2$). (a) $P_a(\mathcal{M})$ *vs.* $\mathcal{M}$. (b) $P_a(\mathcal{A})$ *vs.* $\mathcal{A}$. ψ is a first-order radially symmetric analyzing wavelet. Four different scales $a = 1$, 2, 4, 8 (in σ_W units) are shown. These results correspond to averaging over 32 (1024×1024) images.
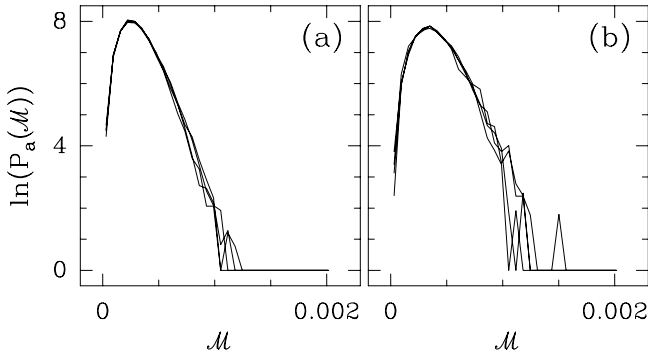
Fig. 22. Pdf's of $\mathcal{M}$ when conditioned by $\mathcal{A}$. The different curves correspond to fixing $\mathcal{A}$ (mod π) to $0 \pm \pi/8$, $\pi/4 \pm \pi/8$, $\pi/2 \pm \pi/8$ and $3\pi/4 \pm \pi/8$. (a) $a = 2^{0.1}$; (b) $a = 2^{1.1}$ (in σ_W units). Same 2D WTMM computations as in Figure 21.
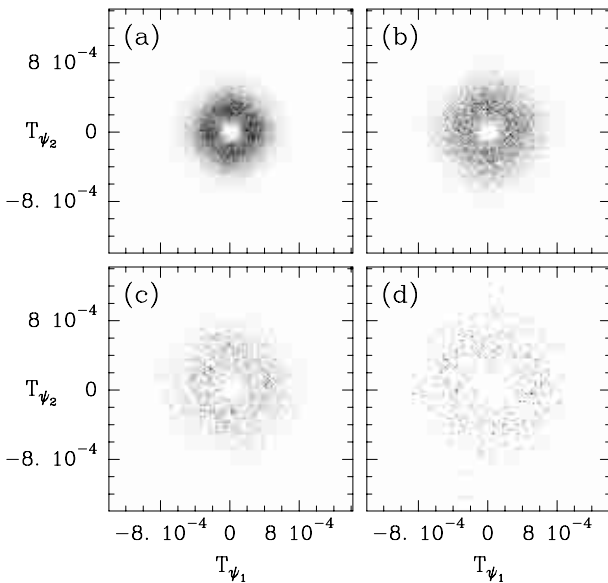
Fig. 23. Distribution of the WTMMM in the plane (T_{ψ_1}, T_{ψ_2}) for the following values of the scale parameter: $a = 1$ (a), 2 (b), 4 (c) and 8 (d) in σ_W units. Same 2D WTMM computations as in Figure 21.
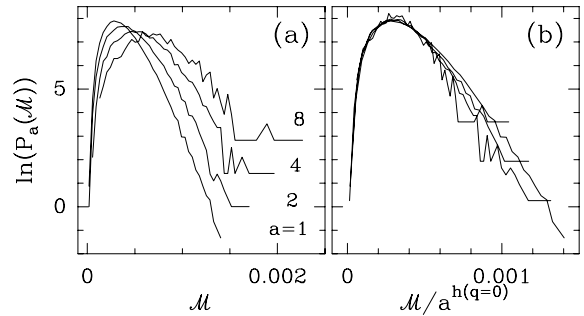
Fig. 24. Pdf's of $\mathcal{M}$ as computed at different scales $a = 1$, 2, 4 and 8 (in σ_W units). (a) $\ln P_a(\mathcal{M})$ *vs.* $\mathcal{M}$. (b) $\ln P_a(\mathcal{M})$ *vs.* $\mathcal{M}/a^{h(q=0)}$ with $h(q = 0) = 0.381$. Same 2D WTMM computations as in Figure 21.

under study. The single-humped $D(h)$ singularity spectrum shown in Figure 16d quantifies statistically the relative contributions of the corresponding singularities of different Hölder exponents.

4 WTMM computation of the self-similarity kernel of multifractal rough surfaces

This section is devoted to the generalization in 2D of the method for determining the self-similarity kernel G originally introduced by Castaing and co-workers [24,82–88] in the context of the analysis of the velocity increment pdf in fully developed turbulent flows. Note that this method has been extended in previous works to the corresponding WTMM pdf [61–63,81,93]. Our goal here is to pave the way from 1D to 2D studies, under some specific assumptions that make this generalization rather straightforward. Our working hypothesis will be the factorization of the joint probability distribution:

$$P_a(\mathcal{M}, \mathcal{A}) = P_a(\mathcal{M})P_a(\mathcal{A}) . \qquad (40)$$

This hypothesis of statistical independence between the modulus and the argument of the WTMMM, is satisfied by construction when investigating the WT skeleton of the multifractal rough surfaces generated with the random $\mathcal{W}$-cascade models discussed in Section 2.2. We will see in paper III [73], that this hypothesis is also quite realistic when analyzing high resolution satellite images of stratocumulus radiance fields [103]. Our strategy will thus consists in computing a kernel G which will account for the evolution of the shape of $P_a(\mathcal{M})$. As far as $P_a(\mathcal{A})$ is concerned, either this distribution is scale independent, as previously observed in Figures 17b and 21b, or it is found to evolve as a function of a (or more likely of $\ln a$) and some important issue will be to explicit the underlying evolution equation (or the underlying dynamical system when dealing with discrete cascading process).

4.1 A method to determine the self-similarity kernel

Under the hypothesis stated in equation (40), Castaing *et al.* ansatz [24,82] can be revisited along the lines drawn in references [61–63], *i.e.*, by taking advantage of the space-scale decomposition provided by the WT skeleton. Because of the implicit assumption of the existence of an underlying multiplicative structure, the WTMMM pdf at a given scale a can be expressed as a weighted sum of dilated pdfs at a larger scale $a' > a$:

$$P_a(\mathcal{M}) = \int G_{aa'}(u) P_{a'}(e^{-u}\mathcal{M}) e^{-u} du , \text{ for } a' > a . \tag{41}$$

For any decreasing sequence of scales $(a_1, ..., a_n)$, the kernel G satisfies the decomposition law:

$$G_{a_n a_1} = G_{a_n a_{n-1}} * ... * G_{a_2 a_1} , \tag{42}$$

where $*$ denotes the convolution product. According to Castaing *et al.* [24,82], the cascade is *self-similar* if there exists a decreasing sequence of scales $\{a_n\}$ such that $G_{a_n a_{n-1}} = G$ is independent of n. The cascade is said *continuously self-similar* [24,82] if there exists a positive, decreasing function $s(a)$ such that $G_{aa'}$ depends upon a and a' only through $s(a, a') = s(a) - s(a')$, *i.e.*, $G_{aa'}(u) = G(u, s(a, a'))$. $s(a, a')$ actually accounts for the number of elementary cascade steps from scale a' to scale a. ($s(a)$ can be seen as the number of cascade steps from the "integral" scale L down to the considered scale a.) In Fourier space, the convolution property (Eq. (42)) turns into a multiplicative property for $\hat{G}$, the Fourier transform of G:

$$\hat{G}_{aa'}(p) = \hat{G}(p)^{s(a,a')} , \text{ for } a' > a . \tag{43}$$

From this equation, one deduces that $\hat{G}$ has to be the characteristic function of an infinitely divisible pdf. Such a cascade is referred to be a *log-infinitely divisible* cascade [21,24]. According to Novikov's definition [21], the cascade is *scale-similar* (or *scale-invariant*) if:

$$s(a, a') = \ln\left(\frac{a'}{a}\right) , \tag{44}$$

i.e., $s(a) = \ln(L/a)$.

Remark

In their original work, Castaing *et al.* [82] have developed a formalism, based on an extremum principle, which turns out to be consistent with the Kolmogorov-Obukhov (1962) general ideas of log-normality [13,14], but which predicts an anomalous power-law behavior of the depth of the cascade. This departure from scale invariance has been confirmed experimentally [61–63,81,93] from the computation of the kernel $G_{aa'}$ of the WTMM pdf which corroborates that $s(a) = ((L/a)^\beta - 1)/\beta$, where β is a Reynolds number dependent exponent which quantifies the deviation from scale-similarity (scale-invariance being ultimately restored for $\beta \to 0$, in the limit of infinite Reynolds number).

Our numerical estimation of G [62,63] is based on the computation of the characteristic function $M(p, a)$ of the WTMMM logarithms at scale a [103]:

$$M(p, a) = \int e^{ip \ln \mathcal{M}} P_a(\mathcal{M}) d\mathcal{M} . \tag{45}$$

From equation (41), it is easy to show that $\hat{G}$ satisfies:

$$M(p, a) = \hat{G}_{aa'}(p) M(p, a') . \tag{46}$$

After the WT calculation and the WTMMM detection, the real and imaginary parts of $M(p, a)$ are computed separately as $< \cos(p \ln \mathcal{M}) >$ and $< \sin(p \ln \mathcal{M}) >$ respectively. The use of the WT skeleton instead of the continuous wavelet transform prevents $M(p, a')$ from getting too small, as compared to numerical noise, over a reasonable range of values of p, so that $\hat{G}_{aa'}(p)$ can be computed from the ratio:

$$\hat{G}_{aa'}(p) = \frac{M(p, a)}{M(p, a')} . \tag{47}$$

4.2 Computing the self-similarity kernel of multifractal rough surfaces generated with random $\mathcal{W}$-cascades

The aim of this sub-section is to perform test applications of our WTMMM methodology to compute the self-similarity kernel using as guinea pigs, the synthetic multifractal rough surfaces generated by the random $\mathcal{W}$-cascade models introduced in Section 2.2.

4.2.1 Uncovering a continuously self-similar cascade

In order to test the validity of equation (43), one first has to focus on the scale dependence of $\hat{G}_{aa'}$ as calculated with equation (47). Figures 25a and 25c respectively show the modulus logarithm $\ln |\hat{G}_{aa'}|$ and the phase $\Phi_{aa'}$, of $\hat{G}_{aa'}$, for various pairs of scales $a < a'$, as computed from the WT skeletons of 32 (1024×1024) images of synthetic log-normal rough surfaces like the one illustrated in Figure 6a. In Figures 25b and 25d respectively, we succeed in collapsing all different curves in Figures 25a and 25c onto a single kernel $\hat{G}(p) = \hat{G}_{aa'}^{1/s(a,a')}$, with $s(a, a') = \ln(a'/a)$ in good agreement with equations (43, 44) and the continuously scale-invariant self-similar cascade picture. Let us point out that this collapse deteriorates for $|p| \gtrsim 5$, as the consequence of finite-size effects as well as of a lack of statistics. As illustrated in Figure 27, similar observations also apply for synthetic log-Poisson multifractal rough surfaces.
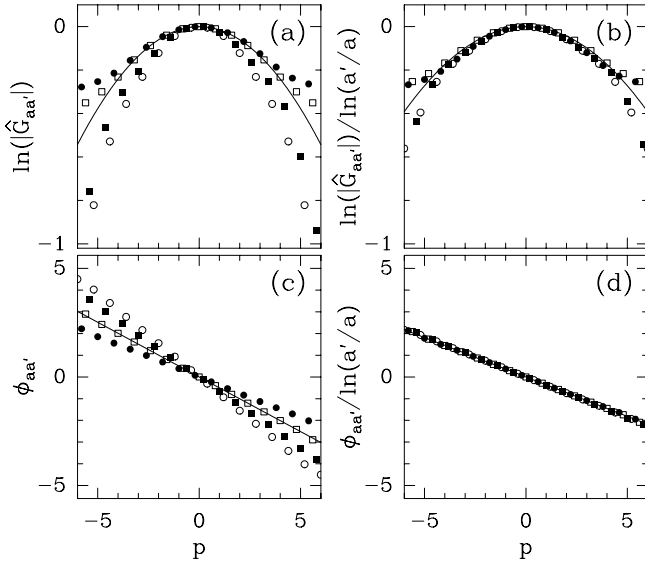
Fig. 25. Estimation of $\hat{G}_{aa'}(p)$ for 32 (1024×1024) images of multifractal rough surfaces generated with the log-normal $\mathcal{W}$-cascade model for the parameter values $m = -0.38\ln 2$ and $\sigma^2 = 0.03\ln 2$. The analyzing wavelet is the first-order radially symmetric wavelet used in Figure 15. (a) $\ln|\hat{G}_{aa'}(p)|$ *vs.* p; (b) $\ln|\hat{G}_{aa'}(p)|/\ln(a'/a)$ *vs.* p; (c) $\Phi_{aa'}(p)$ *vs.* p; (d) $\Phi_{aa'}(p)/\ln(a'/a)$ *vs.* p. The symbols correspond to the following pairs of scale (in σ_W units): $a = 2^{0.5}$, $a' = 2^{3.5}$ ($\circ$), $a = 2$, $a' = 2^{3.5}$ ($\blacksquare$), $a = 2$, $a' = 2^3$ ($\square$), $a = 2^{1.5}$, $a' = 2^3$ ($\bullet$). In (a) and (c), the solid lines correspond to the theoretical predictions for $\hat{G}_{aa'}(p)$ (Eq. (55)) for $a = 2$, $a' = 2^3$ ($\square$). In (b) and (d), the solid lines correspond to the theoretical self-similar kernel $\hat{G}(p) = \exp[(imp - \sigma^2 p^2/2)/\ln 2]$.

4.2.2 Discriminating between log-normal and log-Poisson cascades

The relevance of equation (43) being established, let us turn to the precise analysis of the nature of G. Using the Taylor series expansion of $\ln \hat{G}(p)$ [62,63]:

$$\hat{G}(p) = \exp\left(\sum_{k=1}^{\infty} c_k \frac{(ip)^k}{k!}\right) , \qquad (48)$$

equation (43) can be rewritten as:

$$\hat{G}_{aa'}(p) = \exp\left(\sum_{k=1}^{\infty} s(a,a')c_k \frac{(ip)^k}{k!}\right) , \qquad (49)$$

where the real valued coefficients c_k are the cumulants of G.

Log-normal $\mathcal{W}$-cascade process

Let us come back to the construction rule of the 2D $\mathcal{W}$-cascades defined in Section 2.2. Let P_j the pdf of the wavelet coefficient modulus $d_{j,m,n}$ (Eqs. (24, 25)). Let

$P_j^{(\log)}(u)$ be the pdf of $\ln d_j$:

$$P_j^{(\log)}(u) = e^u P_j(e^u) . \qquad (50)$$

If $j_1 > j_2$, then from equation (28):

$$\ln d_{j_2} = \ln d_{j_1} + \ln M_{j_1-1} + .. + \ln M_{j_2} . \qquad (51)$$

This equation can be rewritten as

$$P_{j_2}^{(\log)}(u) = P_{j_1}^{(\log)} * G_{j_2 j_1}(u) , \qquad (52)$$

where $G_{j_2 j_1}(u) = G*G...*G$, $G(u)$ being the pdf of $\ln M$. In the Fourier space, one gets

$$\hat{P}_{j_2}^{(\log)}(p) = \hat{P}_{j_1}^{(\log)}(p)\hat{G}^{s(j_2,j_1)}(p) , \qquad (53)$$

where

$$s(j_2, j_1) = j_1 - j_2 \qquad (54)$$

represents the number of steps of the cascade from the scale 2^{j_1} to the scale 2^{j_2}. These rather straightforward computations demonstrate the scale-invariance and the self-similarity of the random $\mathcal{W}$-cascades.

In the particular case of a log-normal $\mathcal{W}$-cascade, the self-similarity kernel $G(u)$ is expected to be Gaussian [61–64] which implies the following behavior of the self-similarity kernel in Fourier space:

$$\hat{G}_{aa'}(p) = \exp\left[\left(\frac{imp}{\ln 2} - \frac{\sigma^2 p^2}{2\ln 2}\right)\ln\left(\frac{a'}{a}\right)\right] . \qquad (55)$$

From equation (49), this Gaussian kernel corresponds to the following set of cumulants:

$$c_1 = m/\ln 2 , \ c_2 = \sigma^2/\ln 2 , \ c_k = 0 \text{ for } k \geq 3 . \qquad (56)$$

As shown in Figure 26, those cumulants can be extracted from the behavior of:

$$C_{2n+1}(a, a') = (-1)^n \partial^{2n+1}\Phi_{aa'}/\partial p^{2n+1}|_{p=0} , \qquad (57)$$

and

$$C_{2n+2}(a, a') = \partial^{2n+2}\ln|\hat{G}_{aa'}|/\partial p^{2n+2}|_{p=0} , \qquad (58)$$

for $n \geq 0$, as functions of $\ln(a'/a)$. When plotting $C_1(a, a')$ *vs.* $\ln(a'/a)$, one can see in Figure 26a that for different values of the reference scale a', all the points obtained when varying the scale a fall on a unique straight line which matches perfectly the theoretical prediction $C_1(a, a') = m\ln(a'/a)/\ln 2 = -0.38\ln(a'/a)$. Very good agreement is also found for $C_2(a, a') = \sigma^2 \ln(a'/a)/\ln 2$ in Figure 26b, where the theoretical value $\sigma^2/\ln 2 = 0.03$ provides a nice fit of the slope of the numerical data. In Figure 26c are shown the results for $C_3(a, a')$ which theoretically should be equal to zero (Eq. (56)). Despite some fluctuations resulting from finite-size effects and the lack of statistical convergence, all the data points fall in a rather narrow neighborhood of the horizontal line corresponding to $c_3 = 0$.
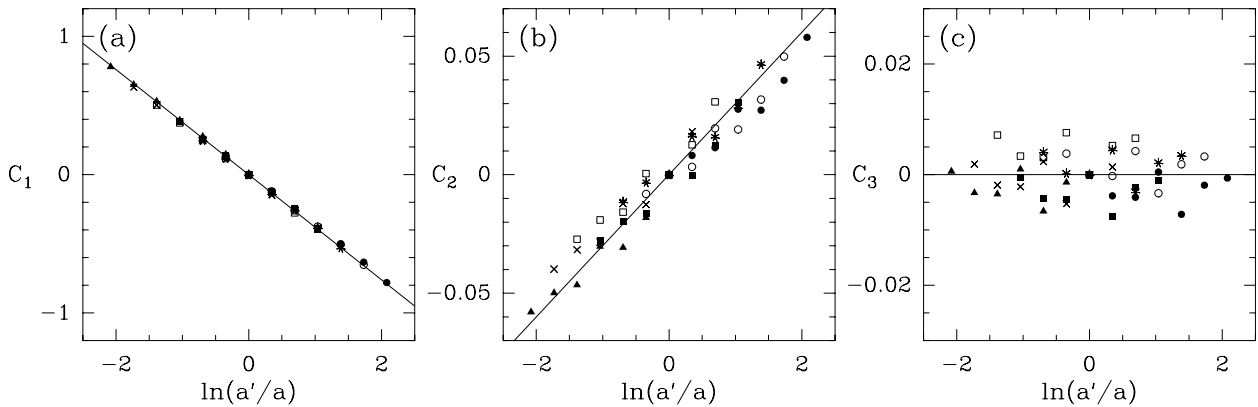
Fig. 26. Computation of the cumulants of the self-similarity kernel $\hat{G}$ of multifractal rough surfaces generated with the log-normal $\mathcal{W}$-cascade model. Same computations as in Figure 25. (a) $C_1(a, a')$ *vs.* $\ln(a'/a)$; (b) $C_2(a, a')$ *vs.* $\ln(a'/a)$; (c) $C_3(a, a')$ *vs.* $\ln(a'/a)$. The symbols correspond to the following values of the reference scale $a' = 2^{0.5}$ (●), 2 (○), $2^{1.5}$ (*), 2^2 (■), $2^{2.5}$ (□), 2^3 (×) and $2^{3.5}$ (▲), in σ_W units. The solid lines correspond to the theoretical slopes $c_1 = m/\ln 2 = -0.38$ (a), $c_2 = \sigma^2/\ln 2 = 0.03$ (b) and $c_3 = 0$ (c).

Log-Poisson $\mathcal{W}$-cascade process

A log-Poisson $\mathcal{W}$-cascade is characterized by the following kernel shape [61–64]:

$$\hat{G}_{aa'}(p) = \exp\left[\left[\frac{\lambda\big(\cos(p\ln\beta) - 1\big)}{\ln 2} + i\frac{\big(\gamma p + \lambda\sin(p\ln\beta)\big)}{\ln 2}\right]\ln\left(\frac{a'}{a}\right)\right], \quad (59)$$

where γ, β and λ are parameters (see Sect. 2.2). This log-Poisson kernel corresponds to the following set of cumulants:

$$c_1 = \frac{\gamma + \lambda\ln\beta}{\ln 2} \text{ and } c_k = \frac{\lambda(\ln\beta)^k}{\ln 2} \text{ for } k \geq 2. \quad (60)$$

Note that the log-Poisson process reduces to a log-normal cascade for $|p\ln\beta| \ll 1$, *i.e.*, in the limit $\beta \to 1$ and $\lambda(\ln\beta)^2 \to \sigma^2$, where the atomic nature of the quantized log-Poisson process vanishes. In Figure 28 are reported the results of the computation of $C_1(a, a')$, $C_2(a, a')$ and $C_3(a, a')$ from the numerical log-Poisson self-similarity kernel $\hat{G}_{aa'}(p)$ shown in Figure 27, for different values of the reference scale a'. In Figures 28a and 28b, all the data points obtained for $C_1(a, a')$ and $C_2(a, a')$, remarkably fall on a straight line when plotted *versus* $\ln(a'/a)$. This is a clear numerical evidence for the scale-similarity of the underlying multiplicative process. Moreover, the slopes of these straight lines are found in very good agreement with the theoretical predictions for the first two cumulants (Eq. (60)): $c_1 = (\gamma + \lambda\ln\beta)/\ln 2 = -0.381$ and $c_2 = \lambda(\ln\beta)^2/\ln 2 = 0.036$. Although we are again faced with finite-size effects and some lack of statistical convergence, when comparing the results obtained for $C_3(a, a')$ in Figure 28c to those reported in Figure 26c for the log-normal $\mathcal{W}$-cascades, one observes a definite tendency of the numerical data to fall about
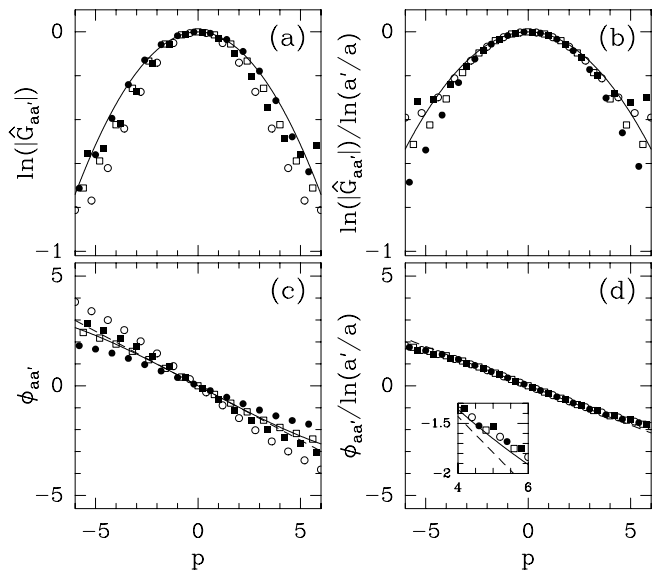
Fig. 27. Estimation of $\hat{G}_{aa'}(p)$ for 32 (1024×1024) images of multifractal rough surfaces generated with the log-Poisson $\mathcal{W}$-cascade model for the parameter values $\gamma = -1/9\ln 2$, $\beta = (2/3)^{1/3}$ and $\lambda = 2\ln 2$. Same representation as in Figure 25. In (a) and (c), the solid lines correspond to the theoretical predictions for $\hat{G}_{aa'}(p)$ (Eq. (59)) for $a = 2$, $a' = 2^3$ (□) in σ_W units; the dashed lines correspond to the log-normal approximation of $\hat{G}_{aa'}(p)$. In (b) and (d), the solid lines correspond to the theoretical self-similar kernel $\hat{G}(p) = \exp\big[\big(\lambda(\cos(p\ln\beta) - 1) + i(\gamma p + \lambda\sin(p\ln\beta))\big)/\ln 2\big]$; the dashed lines correspond to the log-normal approximation $\hat{G}(p) = \exp\big[(i(\gamma + \ln\beta)p - \lambda(\ln\beta)^2 p^2/2)/\ln 2\big]$.

a straight line of negative slope when plotted *versus* $\ln(a'/a)$. This is a strong indication that the third cumulant c_3 is different from zero and that the cascading process is no longer log-normal. Furthermore, as shown in Figure 28c, the theoretical value $c_3 = \lambda(\ln\beta)^3/\ln 2 = -0.0049$ provides a reasonable fit of the data. The relevance of the theoretical self-similarity kernel (Eq. (59)) is
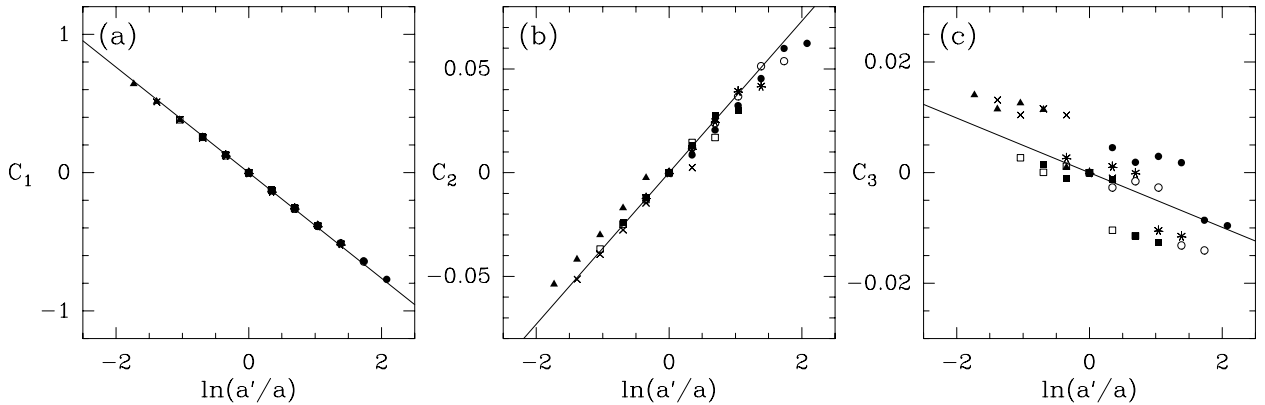
Fig. 28. Computation of the cumulants of the self-similarity kernel $\hat{G}$ of multifractal rough surfaces generated with the log-Poisson $\mathcal{W}$-cascade model. Same computations as in Figure 27. (a) $C_1(a, a')$ *vs.* $\ln(a'/a)$; (b) $C_2(a, a')$ *vs.* $\ln(a'/a)$; (c) $C_3(a, a')$ *vs.* $\ln(a'/a)$. The symbols correspond to the following values of the reference scale $a' = 2^{0.5}$ (●), 2 (○), $2^{1.5}$ (∗), 2^2 (■), $2^{2.5}$ (□), 2^3 (×) and $2^{3.5}$ (▲), in σ_W units. The solid lines correspond to the theoretical slopes $c_1 = (\gamma + \lambda \ln \beta)/\ln 2 = -0.381$ (a), $c_2 = \lambda (\ln \beta)^2 / \ln 2 = 0.036$ (b) and $c_3 = \lambda (\ln \beta)^3 / \ln 2 = -0.0049$ (c).
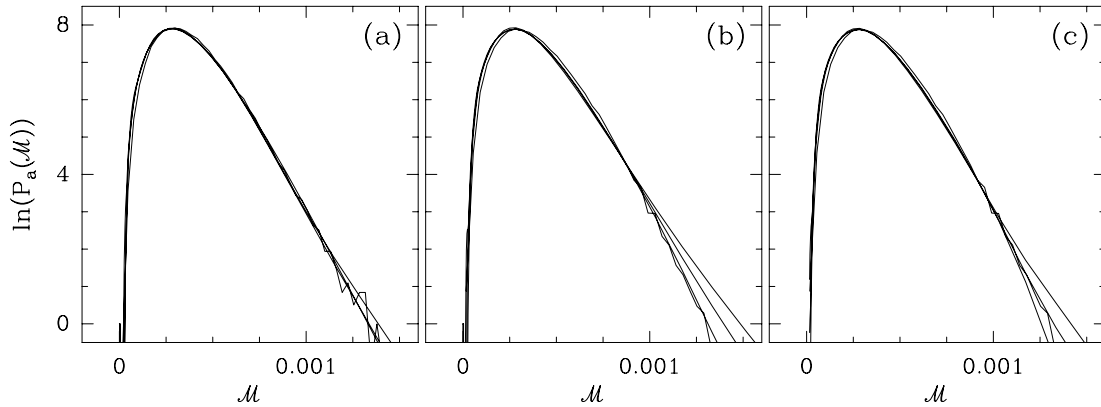
Fig. 29. Pdf's of $\mathcal{M}$ as computed at different scales $a = 1, 2, 4$ and 8 (in σ_W units). (a) $\ln(P_a(\mathcal{M}))$ *vs.* $\mathcal{M}$; same data for log-normal $\mathcal{W}$-cascades as in Figure 20a, after being transformed according to equation (41) with the Gaussian kernel estimated in Figures 25 and 26. (b) $\ln(P_a(\mathcal{M}))$ *vs.* $\mathcal{M}$; same data for log-Poisson $\mathcal{W}$-cascades as in Figure 24a, after being transformed with a Gaussian kernel build from the first two cumulants c_1 and c_2 estimated in Figure 28. (c) Same pdf's as in (b) but after being transformed with a kernel involving the first three cumulants c_1, c_2 and c_3 estimated in Figure 28.

confirmed in Figures 27b and 27d, where the corresponding solid lines are found in good agreement with the data for $-5 \lesssim p \lesssim 5$. Note that the presence of a nonzero third-order cumulant is hardly perceptible in Figure 27d, where the dashed line corresponding to the log-normal linear approximation of $\Phi_{aa'}$ cannot be discarded by the data except for values of $|p| \gtrsim 4$. Unfortunately, for these rather large values of p, one can no longer trust quantitatively our numerical data because of insufficient sampling.

As a check of the reliability of our numerical method to compute the self-similarity kernel $G_{aa'}(u)$, we have succeeded in Figure 29a, in collapsing all the WTMMM pdf's computed at different scales in Figure 20a for log-normal $\mathcal{W}$-cascades, onto a single curve when using the convolution equation (41) with a scale-invariant Gaussian kernel (Eq. (55)). We have tried to do the same remarkable operation for the WTMMM pdf's obtained for the log-Poisson $\mathcal{W}$-cascades in Figure 24a. When using the log-normal approximation of the log-Poisson kernel, taking into account c_1 and c_2 only, one clearly fails in Figure

29b to collapse the right tails of the $\mathcal{M}$ pdf's onto a single curve. When putting into the game the value of the third cumulant c_3 estimated from a linear regression fit of the data in Figure 28c, the collapse is improved but still not perfect because of the statistical uncertainty in our estimate of c_3 when considering a statistical sample of 32 (1024×1024) images only (note that in paper III [73] we will have at our disposal 32 (1024×1024) images of cloudy scenes collected with Landsat satellite).

Remark

From the definition of the characteristic function $M(p, a)$ (Eq. (45)), one gets the following relationship with the partition function $\mathcal{Z}(q, a)$ involved in the multifractal WTMM description (Eq. (70) of paper I [68]) [63]:

$$S(q, a) = \frac{\mathcal{Z}(q, a)}{\mathcal{Z}(0, a)} = \langle \mathcal{M}^q \rangle(a) = M(-iq, a) \,,$$

$$\sim a^{\tau(q)+2} \,, \tag{61}$$

where $\mathcal{Z}(0, a) \sim a^{-2}$, as previously discussed for multifractal rough surfaces that are singular everywhere. From the expression (47) of the Fourier transform of the kernel G and equation (61), one deduces:

$$\frac{S(q, a)}{S(q, a')} = \hat{G}_{aa'}(-\mathrm{i}q) . \tag{62}$$

When further using equation (49), this last equation becomes

$$\frac{S(q, a)}{S(q, a')} = \left(\frac{a'}{a}\right)^{\sum_{k=1}^{\infty} c_k \frac{q^k}{k!}} , \tag{63}$$

which is consistent with the scaling behavior of $S(q, a)$ in equation (61) provided

$$\tau(q) = -\sum_{k=1}^{\infty} c_k \frac{q^k}{k!} - 2 . \tag{64}$$

This general expression for the $\tau(q)$ spectrum reduces to the specific spectra found in equations (29,37), when replacing the cumulants c_k by their respective analytical expressions found in equations (56, 60) for log-normal and log-Poisson $\mathcal{W}$-cascades. Let us note that with the choices of parameter values made in our numerical simulations, the first two cumulants of log-normal ($c_1 = -0.380$, $c_2 = 0.030$) and log-Poisson ($c_1 = -0.381$, $c_2 = 0.036$) $\mathcal{W}$-cascades are so similar that the respective $\tau(q)$ spectra mainly differ by the contribution of the cumulants of order $k \geq 3$. This explains, a posteriori, the difficulties encountered with the 2D WTMM method in Section 3 to distinguish the multifractal spectra of the corresponding log-normal and log-Poisson rough surfaces.

5 Space-scale correlation functions from wavelet analysis

5.1 Space-scale correlation functions

Correlations in multifractals have already been experienced in the literature [104–106]. However, all these studies rely upon the computation of the scaling behavior of some partition functions involving different points; they thus mainly concentrate on spatial correlations of the local singularity exponents. The approach recently developed in references [81,94,97] is different since it does not focus on (nor suppose) any scaling property but rather consists in studying the correlations of the logarithms of the amplitude of a space-scale decomposition of the signal. More specifically, if $\chi(\mathbf{x})$ is a bump function such that $||\chi||_1 = 1$, then by taking

$$\varepsilon^2(\mathbf{x}, a) = a^{-4} \int \chi\left((\mathbf{x} - \mathbf{y})/a\right) \left|\mathbf{T}_\psi[f](\mathbf{y}, a)\right|^2 \mathrm{d}^2\mathbf{y} , \tag{65}$$

one has

$$||f||_2^2 = \iint \varepsilon^2(\mathbf{x}, a)\mathrm{d}^2\mathbf{x}\mathrm{d}a . \tag{66}$$

Thus, $\varepsilon^2(\mathbf{x}, a)$ can be interpreted as the local space-scale energy density of the considered multifractal function $f(\mathbf{x})$. Since $\varepsilon^2(\mathbf{x}, a)$ is a positive quantity, we can define the *magnitude* of the function f at the point $\mathbf{x}$ and scale a as:

$$\omega(\mathbf{x}, a) = \frac{1}{2} \ln \varepsilon^2(\mathbf{x}, a) . \tag{67}$$

Our aim in this section, is to show that a multiplicative process can be revealed and characterized through the correlations of its space-scale magnitudes:

$$C(\mathbf{x}_1, \mathbf{x}_2; a_1, a_2) = \langle\tilde{\omega}(\mathbf{x}_1, a_1)\tilde{\omega}(\mathbf{x}_2, a_2)\rangle, \tag{68}$$

where $\langle...\rangle$ stands for ensemble average and $\tilde{\omega}$ for the centered process $\omega - \langle\omega\rangle$.

Remark

Note that instead of working with the continuous wavelet transform, one can use its skeleton defined by the WTMMM. Within this alternative, the magnitude is simply $\omega(\mathbf{x}, a) = \ln \mathcal{M}(\mathbf{x}, a)$, where the point $(\mathbf{x}, a)$ is by definition a WTMMM.

5.2 Analysis of random $\mathcal{W}$-cascades using space-scale correlation functions

The tree structure of a $\mathcal{W}$-cascade defined on separable wavelet orthogonal basis as explained in Section 2.2, induces correlations between different "details" of the corresponding function $f(\mathbf{x})$ [94–97]. These correlations can be characterized by computing the correlation between two wavelet coefficients at an arbitrary scale $a_j = 2^j$ and at a distance $|\Delta\mathbf{x}| = \Delta x = 2^j\Delta k$, where for the sake of simplicity, we will focus on spatial separations in the x-direction only (we will see later on, that our theoretical predictions are independent of the chosen direction provided the function $f(\mathbf{x})$ displays isotropic scaling properties). Let us fix $\mathbf{k} = (k_x, k_y)$ and let $\mathbf{k}_1 = \mathbf{k}$ and $\mathbf{k}_2 = \mathbf{k} + \Delta\mathbf{k}$, where $\Delta\mathbf{k} = (\Delta k, 0)$. Let us suppose that the last common ancestor (on the quaternary tree of the $\mathcal{W}$-cascade) of the wavelet coefficient modulus $d_{j,\mathbf{k}_1}$ and $d_{j,\mathbf{k}_2}$ (Eqs. (24, 25)) is at a scale $2^{N-l(j,\mathbf{k}_1,\mathbf{k}_2)}$, where in the following $l(j, \mathbf{k}_1, \mathbf{k}_2)$ will be referred as the ultrametric $\mathcal{W}$-distance between two wavelet coefficients [64]. Then, from equation (25), one can write:

$$d_{\mathbf{k}_1} = M^{(N-1)}...M^{\left(N-l(j,\mathbf{k}_1,\mathbf{k}_2)\right)}$$
$$\times M_{[1]}^{\left(N-l(j,\mathbf{k}_1,\mathbf{k}_2)-1\right)}...M_{[1]}^{(j)} , \tag{69}$$

and

$$d_{j,\mathbf{k}_2} = M^{(N-1)}...M^{\left(N-l(j,\mathbf{k}_1,\mathbf{k}_2)\right)}$$
$$\times M_{[2]}^{\left(N-l(j,\mathbf{k}_1,\mathbf{k}_2)-1\right)}...M_{[2]}^{(j)} , \quad (70)$$

where all the $M^{(i)}$, $M_{[1]}^{(i)}$ and $M_{[2]}^{(i)}$ are i.i.d. random variables with the same law $P(M)$ as M. Then their covariance is

$$\mathrm{Cov}(\ln d_{j,\mathbf{k}_1}, \ln d_{j,\mathbf{k}_2}) = \sum_{i=1}^{l(j,\mathbf{k}_1,\mathbf{k}_2)} \mathrm{Cov}\left(\ln M^{(N-i)}, \ln M^{(N-i)}\right)$$
$$= \sigma^2 l(j, \mathbf{k}_1, \mathbf{k}_2), \quad (71)$$

where σ^2 is the variance of $\ln M$. But the ultrametric structure of the $\mathcal{W}$-cascades shows that such a process is not stationary (nor ergodic). Moreover, we will generally consider uncorrelated realizations of size $L = 2^N$ of the same cascade process, so that, in good approximation, the correlation function depends only on the spatial distance $\Delta x = |\Delta\mathbf{x}|$. Thus one can replace ensemble average by space average in the definition of the correlation function [64]:

$$C(\Delta x_{j,2^p}; a_j) = 4^{j-N}\sigma^2 \sum_{l=0}^{l=N-j-1} N_{j,2^p}(l)l , \quad (72)$$

where $N_{j,2^p}(l)$ is the number of wavelet coefficients $d_{j,\mathbf{k}}$ ($0 \leq k_x \leq 2^j - 2^p$) such that $d_{j,\mathbf{k}}$ and $d_{j,\mathbf{k}'}$, where $\mathbf{k} = (k_x, k_y)$ and $\mathbf{k}' = (k_x + 2^p, k_y)$, are at the $\mathcal{W}$-distance l. It is clear that $N_{j,2^p}(l) = 0$ for $l \geq N - j - p$. Moreover, one can easily show that:

$$\forall\, l < N - j - p , \ N_{j,2^p}(l) = 4^p N_{j-p,1}(l) . \quad (73)$$

Since $N_{j,1}(l) = 2^{N-j+l}$, equation (72) becomes ($\forall\, p < N - j$):

$$C(\Delta x_{j,2^p}; a_j) = 4^{j-N}\sigma^2 \sum_{l=0}^{N-j-p-1} 4^p N_{j-p,1}(l)l ,$$
$$= 4^{p+j-N}\sigma^2 \sum_{l=0}^{N-j-p-1} 2^{N-j-p}2^l l ,$$
$$= 2^{p+j-N}\sigma^2 2$$
$$\times \left[(j-p)2^{N-j-p-1} - 2^{N-j-p} + 1 \right] ,$$
$$= \sigma^2(N - j - p - 2 + 2^{p+j-N+1}) . \quad (74)$$

This means that when Δx ($= 2^{p+j}$) is small ($a < \Delta x \ll L$), the correlation function $C(\Delta x, a)$ of a $\mathcal{W}$-cascade behaves as a logarithm function of the spatial distance [64,94]:

$$C(\Delta x, a) \sim \sigma^2 \log_2\left(\frac{L}{\Delta x}\right) . \quad (75)$$

Thus, asymptotically, the correlation function does not depend on the scale a. Moreover, equation (74) is not only valid for spatial separations in the x-direction but also in the y-direction as well as along the diagonals. Therefore equation (75) is likely to apply for isotropic $\mathcal{W}$-cascades after averaging over the direction of $\Delta\mathbf{x}$.

Remark

Using the same kind of computations, one gets that the "two-scale" correlation function $C(\Delta x, a_1, a_2)$, between the WT coefficients at scale a_1 and the coefficients at scale a_2, follows the same law as long as Δx is greater than the supremum of a_1 and a_2, namely [64,94]:

$$C(\Delta x, a_1, a_2) = \sigma^2 \left(\log_2\left(\frac{L}{\Delta x}\right) - 2 + 2\frac{\Delta x}{L} \right) ,$$
$$\text{when } \sup(a_1, a_2) \leq \Delta x < L . \quad (76)$$

Thus, the ultrametric structure of the wavelet representation of multifractal rough surfaces generated with the random $\mathcal{W}$-cascade model, implies that the cross-correlation functions (across scales) decrease very slowly, independently of a_1 and a_2, as a logarithm function of the spatial distance Δx.

5.3 Distinguishing "multiplicative" from "additive" processes underlying the scale invariance properties of rough surfaces

In Figure 30a are reported the results of the computation of $C(\Delta x, a_1, a_2)$ when averaging over 32 (1024×1024) images of multifractal rough surfaces generated with the lognormal $\mathcal{W}$-cascade model for the same parameter values as in Figure 6a. One can see that, for $\Delta x > \sup(a_1, a_2)$, all the data points fall onto a unique curve when plotted versus $\log_2(\Delta x)$, independently of the considered pair of scales (a_1, a_2). Moreover, although the analyzing wavelet is different from the one used in the construction process of the $\mathcal{W}$-cascade, these numerical data are in a striking good agreement with the theoretical prediction given by equation (76) for $\sigma^2 = 0.03 \ln 2$ and $L = 1024$. The observed slow (logarithmic) decay of the space-scale correlation functions is thus a clear signature that magnitudes in random cascades are correlated over very long distances [64,94–97]. Note that both the scale independence and the logarithmic decay are features that are not observed in "additive" models like fractional Brownian motions whose long-range correlations originate from the sign of their variations rather than from the amplitudes. In Figure 30b are plotted the correlation functions $C(\Delta x, a_1, a_2)$ computed from 32 (1024×1024) images of isotropic fractional Brownian surfaces with index $H = 1/3$ (see Fig. 14a of paper I [68]). When comparing with Figure 30a,
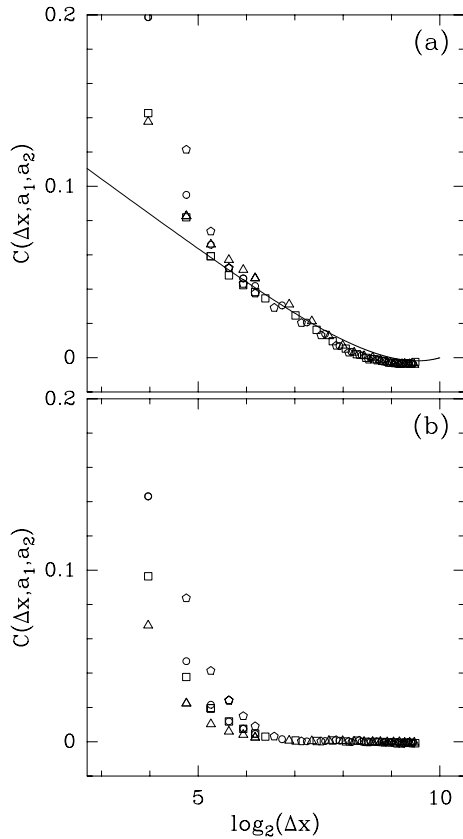
Fig. 30. Magnitude correlation function $C(\Delta x, a_1, a_2)$ *vs.* $\log_2(\Delta x)$, as computed from the continuous wavelet transform of 32 (1024×1024) images. The analyzing wavelet ψ is the radially symmetric first-order wavelet shown in Figure 1 of paper I [68]. (a) Log-normal $\mathcal{W}$-cascades for parameter values $m = -0.38 \ln 2$ and $\sigma^2 = 0.03 \ln 2$. (b) Fractional Brownian surfaces $B_{H=1/3}(\mathbf{x})$. The symbols have the following meaning: $a_1 = a_2 = 2$ ($\circ$); $a_1 = 1$, $a_2 = 2$ ($\triangle$); $a_1 = 1$, $a_2 = 2^2$ ($\square$) and $a_1 = 2$, $a_2 = 2^2$ ($\diamond$) in σ_W units. In (a) the solid line represents the theoretical prediction given by equation (76). We have not shown any data points for $\Delta x \leq \sigma_W$ (~ 13 pixels).

the difference is impressive: for $\Delta x > \sup(a_1, a_2)$, the magnitudes of $B_{H=1/3}(\mathbf{x})$ are found uncorrelated.

Remark

We have reproduced our space-scale correlation analysis for multifractal rough surfaces generated with the log-Poisson $\mathcal{W}$-cascade model. When using the model parameters defined in Figure 6b, one gets numerical data that cannot be distinguished from those shown in Figure 30a for log-normal $\mathcal{W}$-cascades. This can be explained from the fact that the variance parameter $\sigma^2 = \lambda(\ln \beta)^2 = 0.025$ is very close to the value $\sigma^2 = 0.03 \ln 2 = 0.021$ used for generating the log-normal rough surfaces. This is also an indication that in order to discriminate between log-Poisson and log-normal multiplicative processes, one needs to investigate "multi-point" space-scale correlation functions in order to extract information about the higher

moments of the multiplier probability law that governs the $\mathcal{W}$-cascading process.

6 Perspectives

To summarize, we have reported the results of numerical applications of the 2D WTMM method to synthetic multifractal rough surfaces. We have tested the reliability of this method to measure the $\tau(q)$ and $D(h)$ spectra which are at the heart of the multifractal description of multi-affine rough surfaces. We have further proposed a method to compute the self-similarity kernel which provides additional information on the nature of the underlying multiplicative process (*e.g.*, about the multiplier pdf) as well as some subsequent tests of the scale-similarity properties of this process. Finally, we have emphasized the computation of "multi-point" space-scale correlation functions as a decisive test of the existence of magnitude correlations over very long distances as induced by some ultrametric space-scale organization.

Beyond the multifractal description, we have also addressed the very important issue of modeling multi-affine rough surfaces by multifractal functions that are built recursively on separable wavelet orthogonal basis. These 2D random $\mathcal{W}$-cascade models provide some mathematical framework for future theoretical developments concerning the regularity properties of the corresponding random fractal functions. Very much like the rigorous results reported in reference [64] for 1D $\mathcal{W}$-cascades, we hope to elaborate in a forthcoming publication about the actual mathematical link between the $D(h)$ spectrum obtained with the 2D WTMM method, via the Legendre transform of the $\tau(q)$ exponents, and the theoretical singularity spectrum that can be derived analytically from the specific construction rule of the $\mathcal{W}$-cascades. From a practical point of view, we have focused in the present work on some standard isotropic version of the 2D $\mathcal{W}$-cascade with no correlation between the multiplier realizations at each cascade step and no memory effects from one step to the next ones. This rather crude model can be easily modified to incorporate more realistic cascading rules with possible correlations in the branching process that may or may not disturb the isotropic scale invariance properties of the so-constructed rough surface.

Besides the new concepts introduced in this paper, besides its potential theoretical interest, there is a more concrete and technical contribution that is likely to have strong impact on future research. For both image analysis and image synthesis purposes, we have implemented new algorithms and developed new softwares that can be routinely used to analyze as well as to model experimental data. In paper III [73], we will report on the application of our methodology and numerical tools to the analysis of high resolution satellite images of cloudy scenes. This study will bring into light the underlying multiplicative structure of marine stratocumulus clouds. From this diagnostic, we will propose the log-normal isotropic

random $\mathcal{W}$-cascades as a very realistic (at least as compared to commonly used model in literature) model for the intermittent nature of the internal cloud structure. Indeed, through this rather successful application to geophysical data, our message is to emphasize the wide range of potential applications of our 2D wavelet based approach to various domains of fundamental as well as applied sciences. We are convinced that the methodology proposed in the present work will lead to significant progress in the understanding of the mechanisms that underly the formation of rough surfaces in various fields like erosion and corrosion processes, growth phenomena, catalysis, fracture propagation, turbulence, medical imaging and many other areas in physics, chemistry, biology, geology, meteorology and material sciences.

References

1. B.B. Mandelbrot, *Fractals: Form, Chance and Dimensions* (Freeman, San Francisco, 1977); *The Fractal Geometry of Nature* (Freeman, San Francisco, 1982).
2. T.C. Halsey, M.H. Jensen, L.P. Kadanoff, I. Procaccia, B.I. Shraiman, Phys. Rev. A **33**, 1141 (1986).
3. G. Paladin, A. Vulpiani, Phys. Rep. **156**, 148 (1987).
4. C. Meneveau, K.R. Sreenivasan, J. Fluid. Mech. **224**, 429 (1991).
5. H.G.E. Hentschel, Phys. Rev. E **50**, 243 (1994).
6. A.S. Monin, A.M. Yaglom, *Statistical Fluid Mechanics* (MIT Press, Cambridge, MA, 1975), Vol. 2.
7. U. Frisch, *Turbulence* (Cambridge Univ. Press, Cambridge, 1995).
8. L. Richardson, Proc. R. Soc. London, Ser A **110**, 709 (1926).
9. B.B. Mandelbrot, J. Fluid Mech. **62**, 331 (1974).
10. U. Frisch, S. Orzag, Phys. Today, 24 (1990).
11. *Turbulence: A Tentative Dictionary*, edited by P. Tabeling, O. Cardoso (Plenum, New York, 1995).
12. A.N. Kolmogorov, C. R. Acad. Sci. USSR **30**, 301 (1941).
13. A.N. Kolmogorov, J. Fluid Mech. **13**, 82 (1962).
14. A.M. Obukhov, J. Fluid Mech. **13**, 77 (1962).
15. R. Benzi, G. Paladin, G. Parisi, A. Vulpiani, J. Phys. A **17**, 3521 (1984).
16. D. Schertzer, S. Lovejoy, in *Turbulence and Chaotic Phenomena in Fluids*, edited by T. Tatsumi (North-Holland, Amsterdam, 1984).
17. C. Meneveau, K.R. Sreenivasan, Phys. Rev. Lett. **59**, 1424 (1987).
18. D. Schertzer, S. Lovejoy, J. Geophys. Res. **92**, 9693 (1987).
19. S. Kida, J. Phys. Soc. Jpn. **60**, 5 (1990).
20. D. Schertzer, S. Lovejoy, F. Schmitt, Y. Ghigirinskaya, D. Marsan, Fractals **5**, 427 (1997).
21. E.A. Novikov, Phys. Fluids A **2**, 814 (1990); Phys. Rev. E **50**, 3303 (1995).
22. Z.S. She, E.C. Waymire, Phys. Rev. Lett. **74**, 262 (1995).
23. B. Dubrulle, Phys. Rev. Lett. **73**, 959 (1994); J. Phys. II France **6**, 1825 (1996).
24. B. Castaing, B. Dubrulle, J. Phys. II France **5**, 895 (1995).
25. Z.S. She, E. Leveque, Phys. Rev. Lett. **72**, 336 (1994).
26. A. Arnéodo, F. Argoul, J. Elezgaray, G. Grasseau, in *Nonlinear Dynamics*, edited by G. Turchetti (World Scientific, Singapore, 1989), p. 130.
27. A. Arnéodo, F. Argoul, E. Bacry, J. Elezgaray, E. Freysz, G. Grasseau, J.F. Muzy, B. Pouligny, in *Wavelets and Applications*, edited by Y. Meyer (Masson, Paris & Springer Verlag, Berlin, 1992), p. 286.
28. D. Sornette, in *Scale Invariance and Beyond*, edited by B. Dubrulle, F. Graner, D. Sornette (EDP Sciences, Les Ulis & Springer Verlag, Berlin, 1997), p. 235.
29. B.B. Mandelbrot, C. R. Acad. Sci. Paris Ser. A **278**, 289 (1974); 355 (1974).
30. J.P. Kahane, J. Peyrière, Adv. Maths. **22**, 131 (1976).
31. G.M. Molchan, Comm. Math. Phys. **179**, 681 (1996).
32. *Fractals in Geoscience and Remote Sensing, Image Understanding Research Series, Vol. 1, ECSC-EC-EAEC*, edited by G.G. Wilkinson, J. Kanellopoulos, J. Megier (Brussels, Luxemburg, 1995).
33. D. Schertzer, S. Lovejoy, Phys. Chem. Hyd. J. **6**, 623 (1985).
34. S. Lovejoy, D. Schertzer, in Ref. [32], p. 102.
35. *Random Fluctuations and Pattern Growth*, edited by H.E. Stanley, N. Ostrowski (Kluwer Academic, Dordrecht, 1988).
36. J. Feder, *Fractals* (Pergamon, New York, 1988).
37. T. Vicsek, *Fractal Growth Phenomena* (World Scientific, Singapore, 1989).
38. *Fractals in Physics, Essays in honour of B.B. Mandelbrot, Physica D, Vol. 38*, edited by A. Aharony, J. Feder (North-Holland, Amsterdam, 1989).
39. B.J. West, *Fractal Physiology and Chaos in Medecine* (World Scientific, Singapore, 1990).
40. F. Family, T. Vicsek, *Dynamics of Fractal Surfaces* (World Scientific, Singapore, 1991).
41. *Fractals and Disordered Systems*, edited by A. Bunde, S. Havlin (Springer Verlag, Berlin, 1991).
42. *Fractal in Natural Sciences*, edited by T. Vicsek, M. Schlesinger, M. Matsushita (World Scientific, Singapore, 1994).
43. B.J. West, W. Deering, Phys. Rep. **254**, 1 (1994).
44. A.L. Barabási, H.E. Stanley, *Fractal Concepts in Surface Growth* (Cambridge Univ. Press, Cambridge, 1995).
45. *Fractal Aspects of Materials, Material Research Society Symposium Proceeding, Vol. 367*, edited by F. Family, P. Meakin, B. Sapoval, R. Wool (Pittsburg, 1995).
46. J.F. Muzy, E. Bacry, A. Arnéodo, Phys. Rev. Lett. **67**, 3515 (1991); Phys. Rev. E **47**, 875 (1993).
47. E. Bacry, J.F. Muzy, A. Arnéodo, J. Stat. Phys. **70**, 635 (1993).
48. J.F. Muzy, E. Bacry, A. Arnéodo, Int. J. of Bifurcation and Chaos **4**, 245 (1994).
49. A. Arnéodo, E. Bacry, J.F. Muzy, Physica A **213**, 232 (1995).
50. A. Arnéodo, in *Wavelets: Theory and Applications*, edited by G. Erlebacher, M.Y. Hussaini, L.M. Jameson (Oxford Univ. Press, Oxford, 1996), p. 349.

51. R.F. Voss, in *Fundamental Algorithms for Computer Graphics*, edited by R. A. Earnshaw, *NATO Advanced Study Institute, Series E: Applied Science, Vol. 17* (Springer Verlag, Heidelberg, 1985), p. 805; Physica D **38**, 362 (1989).

52. *The Science of Fractal Images*, edited by H.O. Peitgen, D. Saupe (Springer Verlag, New York, 1987).

53. A. Marshak, A. Davis, R. Cahalan, W. Wiscombe, Phys. Rev. E **49**, 55 (1994).

54. T. Vicsek, A.L. Barabási, J. Phys. A: Math. Gen. **24**, L845 (1991).

55. A.L. Barabási, T. Vicsek, Phys. Rev. A **44**, 2730 (1991).

56. J. Eggers, S. Grossmann, Phys. Rev. A **45**, 2360 (1992).

57. J.A.C. Humphrey, C.A. Schuler, B. Rubinski, Fluid Dyn. Res. **9**, 81 (1992).

58. A. Juneja, D.P. Lathrop, K.R. Sreenivasan, G. Stolovitzky, Phys. Rev. E **49**, 5179 (1994).

59. L. Biferale, G. Boffetta, A. Celani, A. Crisanti, A. Vulpiani, Phys. Rev. E **57**, R6261 (1998).

60. R. Benzi, L. Biferale, A. Crisanti, G. Paladin, M. Vergassola, A. Vulpiani, Physica D **65**, 352 (1993).

61. S.G. Roux, Ph.D. thesis, University of Aix-Marseille II, 1996.

62. A. Arnéodo, J. F. Muzy, S.G. Roux, J. Phys. II France **7**, 363 (1997).

63. A. Arnéodo, S. Manneville, J.F. Muzy, Eur. Phys. J. B **1**, 129 (1998).

64. A. Arnéodo, E. Bacry, J.F. Muzy, J. Math. Phys **39**, 4142 (1998).

65. F. Sellan, C. R. Acad. Sci. Paris, Series I: Math. **321**, 351 (1995).

66. P. Abry, F. Sellan, Appl. Computation. Harmonic Analysis **3**, 377 (1996).

67. C. Henegan, S.B. Lowen, M.C. Teich, in Proc. IEEE Southwest Symposium on Image Analysis and Interpretation, San Antonio (1996).

68. A. Arnéodo, N. Decoster, S.G. Roux, Eur. Phys. J. B **15**, 567 (2000).

69. D. Schertzer, S. Lovejoy, in *Fractals: Physical Origin and Consequences*, edited by L. Pietronero (Plenum, New York, 1989), p. 49.

70. J. Wilson, D. Schertzer, S. Lovejoy, in *Scaling, Fractals and Nonlinear Variability in Geophysics*, edited by D. Schertzer, S. Lovejoy (Kluwer, Dordrecht, 1991), p. 185.

71. A. Marshak, A. Davis, W.J. Wiscombe, G. Titov, Remote Sens. Environ. **52**, 72 (1995).

72. A. Davis, A. Marshak, W.J. Wiscombe, R.F. Cahalan, in *Current Topics in Nonstationary Analysis*, edited by G. Treviño *et al.* (World Scientific, Singapore, 1996), p. 97.

73. S.G. Roux, A. Arnéodo, N. Decoster, Eur. Phys. J. B **15**, 765 (2000).

74. I. Daubechies, *Ten Lectures on Wavelets* (S.I.A.M., Philadelphia, 1992).

75. A. Akansu, R. Haddad, *Multiresolution Signal Decomposition* (Academic Press, Boston, 1993).

76. S. Mallat, *A Wavelet Tour in Signal Processing* (Academic Press, New York, 1998).

77. P. Collet, J. Lebowitz, A. Porzio, J. Stat. Phys. **47**, 609 (1987).

78. P. Grassberger, R. Badii, A. Politi, J. Stat. Phys. **51**, 135 (1988).

79. T. Bohr, T. Tèl, in *Direction in Chaos, Vol. 2*, edited by B.L. Hao (World Scientific, Singapore, 1988).

80. A. Arnéodo, F. Argoul, J.F. Muzy, M. Tabard, E. Bacry, Fractals **1**, 629 (1993).

81. A. Arnéodo, S. Manneville, J.F. Muzy, S.G. Roux, Phil. Trans. R. Soc. London A **357**, 2415 (1999).

82. B. Castaing, Y. Gagne, E.J. Hopfinger, Physica **46 D**, 177 (1990).

83. B. Castaing, Y. Gagne, M. Marchand, Physica D **68**, 387 (1993).

84. Y. Gagne, M. Marchand, B. Castaing, J. Phys. II France **4**, 1 (1994).

85. A. Naert, L. Puech, B. Chabaud, J. Peintke, B. Castaing, B. Hebral, J. Phys. II France **4**, 215 (1994).

86. B. Chabaud, A. Naert, J. Peintke, F. Chillà, B. Castaing, B. Hebral, Phys. Rev. Lett. **73**, 3227 (1994).

87. F. Chillà, J. Peintke, B. Castaing, J. Phys. II France **6**, 455 (1996).

88. Y. Malécot, C. Auriault, H. Kahalerras, Y. Gagne, O. Chanal, B. Chabaud, B. Castaing, J. Fluid Mech. (1999), to appear.

89. Y. Gagne, Ph.D. thesis, University of Grenoble, 1987.

90. P. Kailasnath, K.R. Sreenivasan, G. Stolovitzky, Phys. Rev. Lett. **68**, 2766 (1992).

91. P. Tabeling, G. Zocchi, F. Belin, J. Maurer, H. Willaime, Phys. Rev. E **53**, 1613 (1996).

92. F. Belin, P. Tabeling, H. Willaime, Physica D **93**, 52 (1996).

93. A. Arnéodo, S. Manneville, J.F. Muzy, S.G. Roux, Appl. Computational Harmonic Analysis **6**, 374 (1999).

94. A. Arnéodo, E. Bacry, S. Manneville, J.F. Muzy, Phys. Rev. Lett. **80**, 708 (1998).

95. M. Greiner, J. Giesemann, P. Lipa, P. Carruthers, Z. Phys. C **69**, 305 (1996).

96. M. Greiner, J. Giesemann, P. Lipa, Phys. Rev. E **56**, 4263 (1997).

97. A. Arnéodo, J.F. Muzy, D. Sornette, Eur. Phys. J. B **2**, 277 (1998).

98. S. Jaffard, Annals Appl. Probability (1999), to appear.

99. J. Arrault, Ph.D. thesis, Univ. of Bordeaux I, 1995.

100. J. Arrault, A. Arnéodo, A. Davis, A. Marshak, Phys. Rev. Lett. **79**, 75 (1997).

101. A. Davis, A. Marshak, R.F. Cahalan, W.J. Wiscombe, J. Atmos. Sci. **54**, 241 (1997).

102. M. Basseville, A. Benveniste, K.C. Chou, S. A. Golden, R. Nikoukhah, A.S. Willsky, IEEE Trans. Inform. Theory **38**, 766 (1992).

103. A. Arnéodo, N. Decoster, S.G. Roux, Phys. Rev. Lett. **83**, 1255 (1999).

104. M.E. Cates, J.M. Deutsch, Phys. Rev. A **35**, 4907 (1987).

105. A.P. Siebesma, in *Universality in Condensed Matter*, edited by R. Julien, L. Peliti, R. Rammal, N. Boccara (Springer Verlag, Heidelberg, 1988), p. 188.

106. J. O'Neil, C. Meneveau, Phys. Fluids A **5**, 158 (1993).